Master's thesis

NTNU
Norwegian University of Science and Technology
Faculty of Engineering
Department of Marine Technology

Lasse Tellevik

Analyses of ship collisions between an FPSO and an offshore supply vessel

Master's thesis in Marine Technology - Marine Structures
Supervisor: Prof. Jørgen Amdahl and PostDoc Zhaolong Yu
June 2020

NTNU
Norwegian University of
Science and Technology

Lasse Tellevik

Analyses of ship collisions between an FPSO and an offshore supply vessel

Master's thesis in Marine Technology - Marine Structures
Supervisor: Prof. Jørgen Amdahl and PostDoc Zhaolong Yu
June 2020

Norwegian University of Science and Technology
Faculty of Engineering
Department of Marine Technology

NTNU
Norwegian University of
Science and Technology

NTNU
Norges teknisk-naturvitenskapelige universitet
Institutt for marin teknikk

MASTER THESIS 2020
for
Stud. Techn. Lasse Tellevik

Analysis of ship collision between an FPSO and an offshore supply vessel by using Abaqus Explicit solver
Analyse av kollisjon mellom et forsyningsskip og FPSO ved bruk av ABAQUS *eksplisitt*

Overall aim of study:
The object of this study is to run ship collision analyses for a typical FPSO structure by using Abaqus Explicit solver. The striking ship is a typical offshore supply vessel (OSV). The analysis shall be in compliance with the DNVGL-RP-C208 (2017) and company specifications. Both head- on and oblique impacts shall be considered.

Background:

AkerSolutions is using Abaqus Explicit for ship collisions and other types of nonlinear finite element analyses. The advanced material models developed earlier under Ls-Dyna in research community, such as RTCL and BWH failure criteria, are not straightforward to be applied to Abaqus platform. Consequently, there is a need on converting the advanced material models from Ls-Dyna to Abaqus. Additionally, the implementation of the material model into Abaqus shall be in line with the DNVG-RP-C208 (2017), in which the material properties are dependent on the steel sheet thickness and the failure strain is linked to the mesh size. Another challenge is the global rigid body motions for the supply vessel during an oblique impact to the FPSO. The mass inertia and eccentricities shall be considered in the simulation to capture the realistic structure failure.
.
Scope of work:

1) Identify the sources to the deviation between the LS-DYNA and ABAQUS results for crushing of a bow structure against a rigid plate obtained in the project work. Introduce the necessary correction in the modelling/analysis procedure. Focus should especially be placed on the material curve adopted.

2) Discuss the collision scenarios that are relevant for the FPSO and will be simulated. Describe how the resulting damage can be found through simulation with ABAQUS.

3) Implement the BWH material failure criterion including element erosion for failed elements. Verify the failure criterion by comparison with LS-DYNA.

4) Establish a finite element model of the FPSO side structure in the mid ship region. The extent of the model shall take into consideration the collision scenarios that will be analyzed. Discuss thoroughly the choice of boundary conditions. If possible, parameterize the model such that changes to stiffener height, stiffener spacing etc. can be easily

modified.

5) Simulate various collision scenarios using available ship models for the selected scenarios. It is envisaged that skew bow or stern collisions shall be included, where the rigid body motion is simulated with hydrodynamic loads based on potential flow theory or constant added masses and viscous forces. Puncturing of ships side shall be accounted for by the adopted failure criterion and element erosion. Describe the damage to both the side shell of the FPSO and to the impacting ship structure. Compare results with simplified external mechanics formulations according to Z. Lui et.al (2018) *On multi-planar impact mechanics in ship collisions.*

6) Conclusions and recommendations for further work

Literature studies of specific topics relevant to the thesis work may be included.

The work scope may prove to be larger than initially anticipated. Subject to approval from the supervisor, topics may be deleted from the list above or reduced in extent.

In the thesis the candidate shall present his personal contribution to the resolution of problems within the scope of the thesis work.

Theories and conclusions should be based on mathematical derivations and/or logic reasoning identifying the various steps in the deduction.

The candidate should utilize the existing possibilities for obtaining relevant literature.

The thesis should be organized in a rational manner to give a clear exposition of results, assessments, and conclusions. The text should be brief and to the point, with a clear language. Telegraphic language should be avoided.

The thesis shall contain the following elements: A text defining the scope, preface, list of contents, summary, main body of thesis, conclusions with recommendations for further work, list of symbols and acronyms, references and (optional) appendices. All figures, tables and equations shall be numerated.

The supervisor may require that the candidate, in an early stage of the work, presents a written plan for the completion of the work. The plan should include a budget for the use of computer and laboratory resources, which will be charged to the department. Overruns shall be reported to the supervisor.

The original contribution of the candidate and material taken from other sources shall be clearly defined. Work from other sources shall be properly referenced using an acknowledged referencing system.

The report shall be submitted in two copies:

- Signed by the candidate
- The text defining the scope included
- In bound volume(s)
- Drawings and/or computer prints which cannot be bound should be organised in a separate folder.

Supervisor NTNU:
Prof. Jørgen Amdahl
Postdoc Zhaolong Yu

Contact person at Aker Solutions:
PhD Zhenhui Liu

Deadline: June 10 2020

Trondheim, January 15, 2020

Jørgen Amdahl

Abstract

The objective of this master thesis is to study ship collisions for a typical FPSO. The striking vessels are, a standard and an ice-reinforced, modern offshore supply vessel, where the FPSO-side region is subjected to the impact. The size of the offshore supply vessels has increased for the last decades, which leads to higher collision energies than before. The consequences of such collisions have the potential to be catastrophic, especially if the FPSO is severely damaged. Environmental consequences can be colossal, in addition to economic and human factors. It is, therefore, essential to ensure that the structural collision resistance is sufficient.

The analyses are performed with the finite element software Abaqus Explicit. Previous work within this field of study and analytical methods are used for model verification. A simplified coupled analysis method is used, where the added mass factors are assumed constant. A coupled analysis means that the local structural deformation and the external rigid body dynamics are studied simultaneously. A decoupled analysis that separates these two elements is also performed in this thesis. The FPSO is for all analyses fixed, as it is assumed that these rigid body motions are neglectable.

For all analyses, an initial collision energy of 50MJ is assumed, and both head-on and oblique impacts are studied. It is found that the maximum penetration of the FPSO side is 61% of the total side-width, which is caused by the ice-reinforced vessel for head-on impact. It is concluded that there will be no rupture of the inner-side shell; in other words, there will be no catastrophic spill of hydrocarbons.

The offshore supply vessel is found to dissipate the majority of the energy in the collisions. In contrast, the FPSO usually dissipates between 20% and 40%. When struck by the ice-reinforced vessel, the FPSO is found to dissipate less energy than when struck by the standard bow. The most damage caused, regarding both penetration and energy dissipation, occurs for head-on impacts. The dissipated energy decreases for sharper impact angles. For impact angle $45°$, the damage to the FPSO is neglectable when struck by the standard offshore supply vessel.

The comparison between the coupled and decoupled analyses shows that the decoupled analyses predict the energy dissipation to a satisfying degree. The penetration path, on the other hand, show more significant deviations. Especially for sharper impact angles, notable deviations are found. Both these findings correspond well to earlier work within this field of study.

Sammendrag

Målet med denne masteroppgaven er å studere skipskollisjoner for en typisk FPSO. Skipene som kolliderer er, et standard og et is-forsterket, moderne offshore forsyningsskip, der FPSO side-regionen er utsatt for kollisjonen. Størrelsen på offshore forsyningsskipene har økt i løpet av de siste tiårene. Dette fører til høyere kollisjonenergier enn det som var sannsynlig tidligere. Konsekvensene av slike kollisjoner kan potensielt bli katastrofale, spesielt hvis FPSO-strukturen blir alvorlig skadet. De miljømessige følgene kan være enorme, i tillegg til de økonomiske og menneskelige faktorene. Det er derfor viktig å sikre at kollisjonsmotstanden for strukturen er tilstrekkelig.

Analysene utføres med elementmetode programvaren Abaqus Explicit. Tidligere arbeid innen skipskollisjoner er benyttet til å verifisere skipsmodellene som er benyttet, i tillegg til analytiske metoder. En forenklet koblet analysemetode benyttes i denne oppgaven, hvor de hydrodynamiske tilleggsmassene antas konstante. En koblet analyse betyr at den lokale strukturelle deformasjonen og de eksterne skipsbevegelsene analyseres samtidig. En ukoblet analyse som beregner disse to elementene separat blir også utført. FPSO strukturen er for alle analyser antatt fastholdt, ettersom skipsbevegelsene til FPSOen er antatt neglisjerbare.

For alle analyser antas det en kollisjonsenergi på 50MJ, og både rettvinklet og skrå kollisjoner blir analysert. Den maksimale gjennomtrengingen av FPSO-siden er funnet til å være 61% av den totale sidebredden. Dette er forårsaket av det is-forsterkede fartøyet for en rettvinklet kollisjon. Det konkluderes med at det ikke vil være et brudd i de indre sideplatene; med andre ord, det vil ikke være katastrofale utslipp av hydrokarboner.

Offshore forsyningsskipet viser seg å ta opp mest av energien i kollisjonene. FPSOen tar på den andre siden opp mellom 20% og 40% av kollisjonsenergien. Når FPSOen blir truffet av det is-forsterkede fartøyet, blir mindre energi tatt opp av FPSOen, i forhold til når den blir truffet av et standard forsyningsskip. Den største skaden forårsaket av både gjennomtrenging og energiopptagelse, oppstår ved rettvinklede kollisjoner. Mindre energi blir tatt opp av strukturene for skarpere kollisjonsvinkler. For en kollisjonsvinkel på $45°$, er skaden på FPSOen neglisjerbar når den blir truffet av det ikke-forsterkede forsyningsskipet.

Sammenligningen mellom koblede og frakoblede analyser viser at ukoblede analyser forutsier energiopptagelsen i tilfredsstillende grad. Gjennomtrengings-retningen viser derimot mer signifikante avvik. Spesielt for skarpere kollisjonsvinkler er det funnet store avvik. Begge disse funnene samsvarer godt med tidligere arbeid innen dette fagfeltet.

Preface

This master thesis presents the results and work done during the spring semester of 2020. It is written as the final part of the Master of Science degree in Marine Structural engineering at the Norwegian University of Science and Technology(NTNU). This thesis is based on the project thesis work performed in the fall of 2019. The exercise text is formulated by Professor Jørgen Amdahl, who has been the main supervisor.

This report describes the analysis of an offshore supply vessel colliding with an FPSO. The work is done in the FE-software Abaqus Explicit. Relevant theory, modeling considerations, and results for different collision scenarios will be presented. A comparison between a coupled and decoupled method is also included.

At times, the work has been challenging, as most of the software and theory were new to me. However, writing this thesis has been an overall good experience. I have obtained much new knowledge within this thesis scope, and more general academic work experience that will be valuable in the future.

During this spring, I've received help from several people, who has been crucial to the final result. I want to thank my supervisor Professor Jørgen Amdahl for his help and guidance during the whole semester. My co-supervisor PostDoc Zhaolong Yu for his support with modeling in Patran and the use of the high-performance computer Vilje. I am also very grateful to Professor Mihkel Korgesaar at TalTech University, who let me use his material model. His help and willingness to help with the BWH-fracture model implementation is highly appreciated. Ph.D. Zhenhui Liu at Aker Solutions has provided valuable feedback regarding the external mechanics model and Ph.D. candidate at NTNU, Woongshik Nam, who has given helpful advice regarding the use of Abaqus in Vilje.

Lasse Tellevik
Tromøya, June 2020

Table of Contents

List of Tables

List of Figures

Nomenclature

This nomenclature should give the requisite naming scheme used for different properties and dimensions in this report. Unless where otherwise stated, all values are given in SI units.

Abbreviations

ALS	Accidental Limit State
BWH	Bressan-Williams-Hill fracture criterion
COG	Center Of Gravity
DNV	Det Norske Veritas
DOF	Degree of Freedom
DP	Dynamic Positioning
DWT	Deadweight Tonnage
FEA	Finite Element Analysis
FEM	Finite Element Method
FLD	Forming Limit Diagram
FPSO	Floating Production Storage and Offloading
LRFD	Load and Resistance Factor Design
NCS	Norwegian Continental Shelf
OSV	Offshore Supply Vessel
PDE	Partial Differential Equation
RTCL	Rice-Tracey and Cockroft-Latham fracture criterion

Symbols

α	angle
β	Frame angle
β'	Normal frame angle
$\ddot{s}$	Acceleration
Δ	Mass displacement
δ	Strain length
$\dot{\varepsilon}$	Strain rate
ϵ	Permutation tensor
γ_f	Partial factors for actions
γ_M	Material factor
$\mathbf{C}$	Damping matrix
F_{ext}	External force
I	Inertia matrix
$\mathbf{K}$	Stiffness matrix or Collision matrix
$\mathbf{M}$	Mass matrix

$\mathbf{R}$	Force vector
$\mathbf{r}$	Displacement vector
$\mathbf{T}$	Transformation matrix
u	Displacement vector
μ	Friction factor
ν	Poisson ratio
ω	Eigenfrequencies
ρ	Density
σ	Stress
τ	Shear stress
θ	Angle between to colliding ships
ε	Strain
A	Cross-section area
a	Added mass
A_{wp}	Waterplane-area coefficient
C_b	Block coefficient
C_m	Midship coefficient
dw_s	Equivalent displacement
E	Energy or Youngs modulus
E_a	Energy dissipation from analytical calculation
E_i	Energy dissipation in the principal directions
E_k	Kinetic energy
E_s	Strain energy
E_{fpso}	Energy dissipated by FPSO
E_{osv}	Energy dissipated by OSV
f	Interaction force
g	Gravitation
K	Hardening parameter
L_{pp}	Length between perpendiculars
m	Mass
n	Hardening parameter
r_b	Impact position in body fixed coordinate system
R_d	Design resistance
R_s	Reaction force
R_{ii}	Radius of gyration
S	Impulse
S_d	Design action effect
S_k	Characteristic action effect
u, v, r	Velocity

1 Introduction

1.1 Background

A floating production storage and offloading(FPSO) unit is a vessel that produces, processes, and store hydrocarbons. FPSOs can be purpose-built ship structures, spar platforms, other geometries, as well as converted tankers. In this thesis, the focus will be on a typical FPSO ship structure. These vessels are effective installations for remote and deepwater locations where pipelines are expensive. In addition, the vessels can be moved to new fields when the current field is depleted, which makes it possible for marginal field development. At the Norwegian Continental Shelf(NCS), there are eight FPSOs today.

Collisions with supply vessels, passing merchant vessels, and shuttle tankers are considered major threats to FPSOs. However, the consequences of such events can be substantial, as FPSOs have a large storage capacity for hydrocarbons. A hydrocarbon leakage can be catastrophic, as well as the economic consequences of loss of production and structural integrity. Therefore it is essential to consider such events when designing such structures.

In recent years, the displacement of the supply vessels has increased. More ships utilize bulbs than before, as well as other bow-shapes such as the X-bow. Dynamic Positioning(DP) and autopilot systems can also lead to higher collision velocities if these systems fail. These factors lead to a significant increase in design collision energy compared to what was previously utilized. Many FPSOs on the NCS were newbuilds in the late 90s, which means that the structures are close to their original lifetime. If prolonging operations for these structures are wanted, a lifetime extension may be needed. In this case, it is important to consider the increased design collision energy.

There were 115 collisions reported on the NCS in the period 1982-2010, according to Kvitrud (2011), and 26 of them were reported in the period 2001-2010. Two of the most critical events are the Far Symphony collision with West Venture in 2004, seen in Figure 1.1, and the Big Orange XVIII collision with Ekofisk in 2009 seen in Figure 1.2. These events had a collision energy of $39MJ$ and $70MJ$, respectively. Moan et al. (2019) proposed, based on these collisions and other data, to increase the minimum bow impact energy design value for supply vessels from $11MJ$ to $50MJ$.

Figure 1.1: Damage on Far Symphony to the left, and West Venture to the right after collision in 2005. Picture from Pettersen and Soegaard (2005).

Figure 1.2: Damage on Big Orange XVIII to the left, and Ekofisk 2/4-P to the right after collision in 2009. Picture from Bjørheim (2017).

1.2 Objective

This thesis's objective is to describe the energy dissipation and structural deformation in a collision between an offshore supply vessel(OSV) and an FPSO. Both head-on and oblique impacts will be considered, as well as different drafts of the FPSO. An ice-strengthened bow OSV-bow with the same principal dimensions as the OSV will also be studied. The analysis is performed in the FE-software Abaqus Explicit, but also simplified analytical method is utilized for comparison and verification. Both a decoupled and a coupled approach is used. The most critical scenarios will be discussed, where

penetration of the FPSO-side, in general, is the structural response with the most substantial consequences. The results will be verified by comparing the results to simplified analytical methods. Other researchers' work will also be central for verification.

Relevant theory within collision mechanics, non-linear finite element analysis, and fracture models will be presented. The modeling of the FPSO-side in the software Patran, as well as the set-up and choices made for the impact analyses in Abaqus, will be discussed.

1.3 Scope and limitations

The initial scope of this thesis work is presented in the first pages of this thesis. This scope origins from the project thesis work done as a preparation for this thesis. Some points have been studied extensively, while others are decided to have a more brief focus. There have also been done some work outside the initial scope. The most notable additions are the analysis of an ice-strengthened OSV-bow and comparisons between coupled and decoupled methods. Choices made regarding the final scope of this thesis have been determined in agreement with the supervisor.

A simplified coupled approach was used for the coupled analyses by utilizing constant added mass coefficients. However, there have been developed methods for including transient hydrodynamic effects in the finite element code in the last years without the need for external routines. It is possible to create a subroutine for a full coupled method in Abaqus, but this was not prioritized because of time limitations. Other ship models, such as a tanker or a stern-model, could have been studied if there was more time.

It should be noted that the first point of the thesis text was decided not to be discussed in particular in this thesis. This point was concerning the verification of the load-deformation curve for an OSV-bow colliding in a rigid wall. This originates from the project thesis work done by the author. In the project thesis, there were significant deviations from the verification curve utilized. The cause was discovered early in this thesis work and was found to be a combination of boundary conditions, fracture modeling, and material properties. As this was solved at an early stage, it was decided that it was sufficient for this thesis with a regular discussion regarding the verification of the load-deformation curve.

1.4 Thesis organization

Chapter 1 - Introduction
The background of this thesis, objective, scope and limitations, and the thesis organization are described.

Chapter 2 - Principles of analysis of accidental impacts
Defines the accidental limit state and the head-on ship collision impact design load.

Chapter 3 - Impact mechanics
Presents relevant theory regarding ship collision. Important keywords are energy dissipation, external dynamics, internal mechanics, and coupled analysis of rigid body motions and local structural damage.

Chapter 4 - Theory of Finite Element Analysis
Describes both linear and non-linear finite element analysis, with a primary focus on the non-linear part. The material fracture models used in this thesis will be presented. The theory behind the solving techniques utilized for FE-analyses in general and in specific Abaqus Explicit are also presented in this section.

Chapter 5 - Finite element models and analysis set-up
Describes the finite element models used in this thesis, a standard bulbous OSV-bow, an ice-reinforced OSV-bow, and an FPSO-side. The OSV-models are pre-existing models, and the FPSO-model is created by the author. The modeling description of the latter will therefore be more thorough. The material model, verification of the model, and analysis scenarios are also presented in this section.

Chapter 6 - Analysis of Ship Collision
Presents the results obtained in this thesis. Topics discussed will be differences in impact angle, FPSO load condition, and the effect of an ice-reinforced bow. A comparison of coupled and decoupled analyses will also be presented. It was decided, in consultation with the supervisor, to include relevant discussion topics in this section. This was decided to improve the readability of the results.

Chapter 7 - Conclusions and further work
The main findings and concluding remarks of this thesis. It also includes possible error sources and recommendations for further work.

2 Principles for analysis of accidental impacts

Ship collision design is governed by the Accidental Limit State(ALS). This limit state is defined as the loads corresponding to an annual exceedance probability of 10^{-4}. The purpose of this limit state is to make sure that the complete integrity of the structure is not lost. According to DNVGL-OS-C101 (2018), a structure exposed to accidental loads should be checked in two steps. The first step is to check if the structure can withstand the design accidental events, with neglectable damage. If step one leads to failure, step two is to check the damaged structure for the resistance of a one-year environmental condition without loss of floatability, stability, or global structural integrity. The ALS include among others:

- explosions and fires
- ship impacts
- dropped objects

2.1 Ship collision design value

The requirements for collisions from offshore supply vessels were updated in the 1980s by DNV. The minimum impact action energy was defined to be $11MJ$ and $14MJ$ for head-on and side-impact, respectively. These values origins from an impact speed of $2m/s$ and the maximum size of supply vessels that serviced the installation. At that time, the majority of the supply vessels had DWT(Deadweight Tonnage) between 1000 and 2000 tonnes and a maximum size of approximately 3000 tonnes. In 2013, the mean size had increased to 4000-5000 DWT and a maximum size of 8000 DWT (Moan et al., 2019). From high-energy collisions that have occurred in the North Sea after the year 2000, it can be seen that the impact speed often is higher than $2m/s$. For example, in the Big Orange XVIII collision at the Ekofisk field in 2009, where the impact speed is estimated to be as high as $4.5m/s$(Moan et al., 2019). The increase in impact speed can origin from the increased use of dynamic positioning and more powerful engines on the supply vessels. In addition to the increase in the mentioned magnitudes, the design of the supply vessels has changed. Many vessels now have ice-strengthened hulls, and some ships use different bow designs, such as the X-bow design. This means that many older offshore installations may not be sufficiently designed against the current collision energy scenarios. The new ALS design action effect for bow impact is based on the factors discussed above and determined to be $50MJ$(Moan et al., 2019).

The general safety criterion is based on the Load and Resistance Factor Design method (LRFD)(DNVGL-RP-C204, 2017) and can be expressed as

$$S_d \leq R_d \tag{2.1}$$

where

S_d = $S_k \gamma_f$, Design action effect
$R_d = \frac{R_k}{\gamma_M}$, Design resistance
$S_k =$ Characteristic action effect
$\gamma_f =$ Partial factors for actions
$R_k =$ Characteristic resistance
$\gamma_M =$ Material factor taking material properties, failure consequence and model uncertainties into account.

For ALS γ_f and γ_M is equal to 1.0, hence $R_d > 50MJ$ for bow impacts.

For collision analyses, a low percentile material strength for the struck vessel is a reasonable assumption. The material of the striking ship is assumed to be the mean percentile of the material, according to DNVGL-RP-C208 (2016). If a high percentile material had been assumed, the annual probability, according to Storheim et al. (2018), would be much lower than 10^{-4}, which is the ALS condition. The material data used in this thesis can be found in Section 5.3.

3 Impact mechanics

According to the law of energy conservation, the total energy of an isolated system remains constant at all times. For a ship collision scenario, the initial kinetic energy will be transformed into final kinetic energy, strain and heat energy, and some wave damping effects. The initial kinetic energy is governed by the mass, added mass, and velocity of both structures at impact.

The most used analysis method for ship collisions in the past has been to decouple the problem into two separate processes, external dynamics and internal mechanics(Liu and Amdahl, 2010). The external dynamics take into account the rigid body motions and determine the amount of energy dissipated as strain energy in the striking and struck vessels. The internal mechanics is concerned with the strain energy distribution for the two vessels. This involves large deformations that are analyzed by simplified plastic theory or by non-linear FEA. A simplified decoupled solution method was first introduced by Minorsky (1959).

The distribution of strain energy is distinguished between strength design, ductility design, and shared-energy design according to the design principles for ship collisions in DNVGL-RP-C204 (2017). This is shown in Figure 3.1.

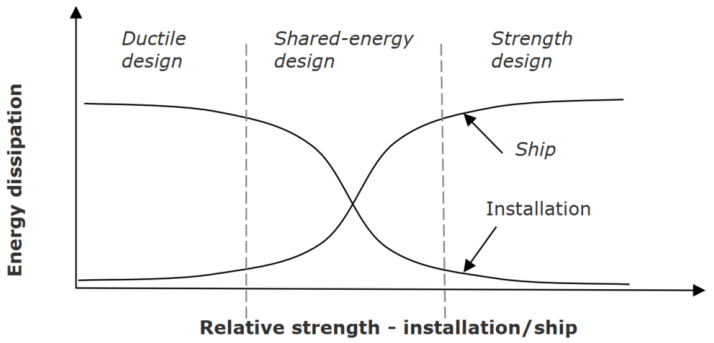

Figure 3.1: Energy dissipation for strength ductile and shared-energy design (DNVGL-RP-C204, 2017).

Strength design implies that the installation is strong enough to resist the collision force with minor deformation. This means that the striking vessel is forced to dissipate most of the energy. Ductility design implies, on the other hand, that the struck installation

dissipates most of the energy. Hence large plastic deformations occur in the installation. In shared-energy design, both vessel and installation undergoes significant deformations and contribute significantly to energy dissipation. In strength and ductility designs, one of the structures will be assumed rigid for the whole impact period. Hence the calculations are less complicated. When these design principles can not be assumed, the shared-energy design is used. In this design, both the magnitude and distribution of collision force depends on the deformation of both structures (NORSOK-N001, 2004). In most cases, shared-energy or ductile design is assumed. For specific cases, the strength design principles can be utilized with only minor changes in the structure.

3.1 External dynamics

The external dynamics is governed by the conservation of momentum and the conservation of energy. For maximum possible energy dissipation, the collision is occurring at the COG of the ship, and striking ship is perpendicular to the ship-side. Assuming a perfectly inelastic collision, the 1 DOF conservation of momentum expression can be expressed as

$$(m_s + a_s)v_s + (m_i + a_i)v_i = (m_s + m_i + a_s + a_i)v_f, \tag{3.1}$$

where m, a, and v express the mass, added mass, and velocity, respectively. The subscripts separate between ship(s) and installation(i). In this thesis, the OSV and FPSO represent the ship and installation. The final joint velocity is noted v_f.

Equation 3.1 can then be solved for v_f

$$v_f = \frac{(m_s + a_s) + (m_i + a_i)v_i}{(m_s + m_i + a_s + a_i)}. \tag{3.2}$$

This expression can be utilized in the equation for the conservation of energy. The left side of this equation consists of the kinetic energy for the two vessels, while the right side consists of the kinetic energy for the connected structure after the collision and the energy dissipated in the collision, E_s. This equation is shown below.

$$\frac{1}{2}(m_s + a_s)v_s^2 + \frac{1}{2}(m_i + a_i)v_i^2 = \frac{1}{2}(m_s + m_i + a_s + a_i)v_f^2 + E_s \tag{3.3}$$

By solving Equation 3.3 for E_s an expression for the dissipated energy is obtained as seen in Equation 3.4.

$$E_s = \frac{1}{2}(m_s + a_s)v_s^2 \frac{(1 - \frac{v_i}{v_s})^2}{1 + \frac{m_s + a_s}{m_i + a_i}}. \tag{3.4}$$

This is the equation presented in the design principles for ship collisions in DNVGL-RP-C204 (2017), where it is applicable for compliant structures. A structure is defined as compliant if the duration of impact is small compared to the fundamental period of vibration of the installation. This assumption is reasonable for an FPSO which have natural periods in all degrees of freedom above 20s(DNVGL-RP-F205, 2017).

3.2 New external dynamic formulation

A new formulation for impact mechanics of ship-collisions were presented by Liu and Amdahl (2010) and extended in Liu and Amdahl (2019) which is based on theories presented by Pedersen and Zhang (1998) and Stronge (2004). The main steps of the calculation procedure is described in this section, and the full derivation can be found in Liu and Amdahl (2019).

Three different coordinate systems are defined to derive the equations of motion. There are the global coordinate systems for the two colliding ships, XYZ, and X'Y'Z' respectively. These systems origins in each of the ships COG at the time of the impact as this will reduce the effect of COG movement to a minimum. In addition to the two global coordinate systems, a local coordinate system, $n_1 n_2 n_3$, is located at the contact point C. In this system, n_1 has a direction parallel to the contact surface, and n_3 is perpendicular to the contact surface. These coordinate systems are shown in Figure 3.2.

The assumption of coordinate system origin in the ship COG makes it possible to assume that the mass and inertia matrices are diagonal. Also, the symmetry properties of the ships can make the expressions significantly less complicated, which in the end will make the method more computer efficient.

To calculate the energy dissipation, the local coordinate system is used as a common coordinate system for the two ships. This means that a transformation matrix between the global coordinate system and the local system at the contact point is utilized. It is assumed that the hull shape of ship A determines the orientation of the local frame. The hull shape angles that are utilized are defined by DNVGL-RU-Ship-Pt.6-Ch.6 (2019), and is shown in Figure 3.3. It is therefore convenient to choose the ship with the less complex surface at impact point as ship A. For example, for a head-on impact, bow against ship-side, the latter would be chosen as ship A.

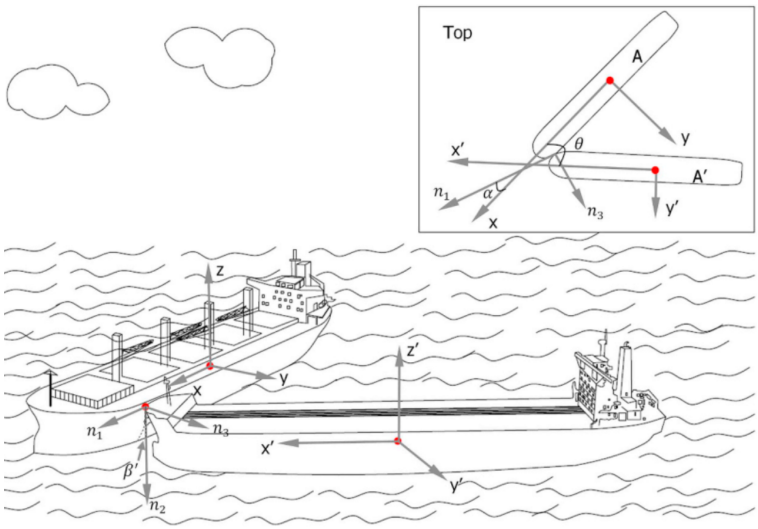

Figure 3.2: Illustration of a ship-ship collision. The superscript ' indicates ship number 2, and respective coordinate system. Figure from Liu and Amdahl (2019)

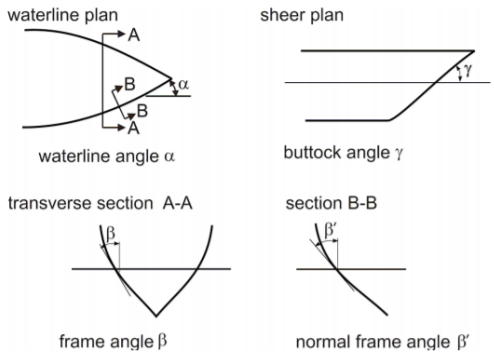

Figure 3.3: Hull angles defined from DNVGL-RU-Ship-Pt.6-Ch.6 (2019)

The direction cosines for the parallel direction for ship A can then by simple trigonometric evaluation be expressed as

$$cos(\vec{n_1}X) = cos(\alpha) \tag{3.5}$$

$$cos(\vec{n_1}Y) = -sin(\alpha) \tag{3.6}$$

$$cos(\vec{n_1}Z) = 0 \tag{3.7}$$

For example, the angle between n_1 and Z is always 90°, which is reasonable as n_1 is always parallel to the waterline. The direction cosines for the normal direction, n_3, can be found in the same way and is shown in row 3 in Equation 3.8. The direction cosines in direction n_2 is found by the cross-product of n_1 and n_3. This results in the transformation matrix for ship A seen in Equation 3.8.

$$T_b^n = \begin{bmatrix} \cos(\alpha) & -\sin(\alpha) & 0 \\ -\sin(\alpha)\sin(\beta') & -\cos(\alpha)\sin(\beta') & -\cos(\beta') \\ \sin(\alpha)\cos(\beta') & \cos(\alpha)\cos(\beta') & -\sin(\beta') \end{bmatrix} \tag{3.8}$$

A special case is when the striking ship collides midship. In this situation $\alpha = \beta = \beta' = 0$ which gives the very simple transformation matrix:

$$T_b^n = \begin{bmatrix} 1 & 0 & 0 \\ 0 & 0 & -1 \\ 0 & 1 & 0 \end{bmatrix}. \tag{3.9}$$

The transformation matrix for Ship A to A' is found by utilizing the angle θ seen in Figure 3.2. This leads to the transformation matrix from :

$$T_b^{b'} = \begin{bmatrix} \cos(\theta) & \sin(\theta) & 0 \\ -\sin(\theta) & \cos(\theta) & 0 \\ 0 & 0 & 1 \end{bmatrix}. \tag{3.10}$$

Then the transformation matrix from the global coordinate system of ship A' to the local system can be expressed as

$$T_{b'}^n = T_b^n T_{b'}^b. \tag{3.11}$$

The velocities are defined for each of the ships in its body-fixed coordinate system. The respective transformation matrices are then used, which lead to an expression for an initial relative velocity, $\bar{v}_n^0$, in the local coordinate system. This is shown in Equation 3.12

$$\bar{v}_n^0 = T_b^n \cdot v_b^0 - T_{b'}^n \cdot v_{b'}^0 \tag{3.12}$$

The impact location is then defined for both body-fixed coordinate system as $r_b = (x, y, x)$ and $r_[b'] = (x', y', z')$ respectively. These are then used to obtain the lever arm matrix **D**, which is shown for ship A in the equation below:

$$D_n == T_b^n \cdot r_b^* \tag{3.13}$$

where r_b^* is defined as

$$T_b^{b'} = \begin{bmatrix} 0 & -r_{b,z} & r_{b,y} \\ r_{b,z} & 0 & -r_{b,x} \\ -r_{b,y} & r_{b,x} & 0 \end{bmatrix}. \tag{3.14}$$

The 3x3 collision matrix for ship A, $\mathbf{K_n}$ can now be expressed as follows:

$$K_{ij} = \frac{T_b^n(i,1)T_b^n(j,1)}{(1+a_1)M} + \frac{T_b^n(i,2)T_b^n(j,2)}{(1+a_2)M} + \frac{T_b^n(i,3)T_b^n(j,3)}{(1+a_3)M} + \tag{3.15}$$

$$\frac{D_n(i,1)D_n(j,1)}{(1+a_4)MR_{xx}^2} + \frac{D_n(i,2)D_n(j,2)}{(1+a_5)MR_{yy}^2} + \frac{D_n(i,3)D_n(j,3)}{(1+a_5)MR_{zz}^2} \tag{3.16}$$

where a_i is the added mass coefficients, $R_i i$ is the radii of gyration and M is the mass of the ship. Equation 3.15 are also applied for ship A'. The added mass coefficients and radii of gyration are based on the expressions derived by Popov et al. (1969) which can be seen in Appendix A. The final collision matrix, $\bar{\mathbf{K}}_\mathbf{n}$ is then assembled by adding K_n and K_n'.

An impulse vector, **S**, is calculated to obtain friction factors needed for the tangential motions in the collision. This vector describes the impulse in each direction of the local coordinate system and is calculated as follows:

$$S = K_n^{-1} \cdot dv \tag{3.17}$$

where the relative velocity change during impact **dv** is equal to $[\bar{v}_1^0$,-$\bar{v}_2^0$, $-(1+e)\bar{v}_r^0]^T$ when there are no sliding motion. The restitution factor, *e*, is the ratio between the raltive velocities in the local coordinate system local direction after and before the impact. The friction factors are defined as:

$$\mu_n = sign(S_1)\frac{\sqrt{S_1^2 + S_2^2}}{S_3}, \quad \mu_t = \frac{S_2}{S_1}, \quad \mu_1 = \frac{S_1}{S_3}, \quad \mu_2 = \frac{S_2}{S_3} \tag{3.18}$$

The dissipated energy in each direction of the local coordinate system can then be expressed:

$$E_1 = \frac{1}{2}\frac{\mu_1}{\mu_1 \bar{K}_{n,(1,1)} + \mu_2 \bar{K}_{n,(1,2)} + \bar{K}_{n,(1,3)}}(v_1^0 - v_1^{0'})^2 \tag{3.19}$$

$$E_2 = \frac{1}{2}\frac{\mu_2}{\mu_1 \bar{K}_{n,(2,1)} + \mu_2 \bar{K}_{n,(2,2)} + \bar{K}_{n,(2,3)}}(v_2^0 - v_2^{0'})^2 \tag{3.20}$$

$$E_3 = \frac{1}{2}\frac{1}{\mu_1 \bar{K}_{n,(3,1)} + \mu_2 \bar{K}_{n,(3,2)} + \bar{K}_{n,(3,3)}}(1 - e^2)(v_3^0 - v_3^{0'})^2 \tag{3.21}$$

Assuming no tangential velocity change and a restitution factor equal to zero, E_3 can be written as

$$E_3 = \frac{1}{2}\frac{1}{\bar{K}_{n,(3,3)}}(v_3^0 - v_3^{0'})^2. \tag{3.22}$$

Equation 3.22 is now on the same form as the simplified Equation 3.4, but is applicable for head-on and oblique impacts in all 6DOF.

3.3 Internal mechanics

After the total strain energy dissipation is found from the external mechanics considerations, the energy distribution between the two vessels can be estimated. The structural response in the structures can be found by using a load-deformation relation. An example of this can be seen in Figure 3.4.

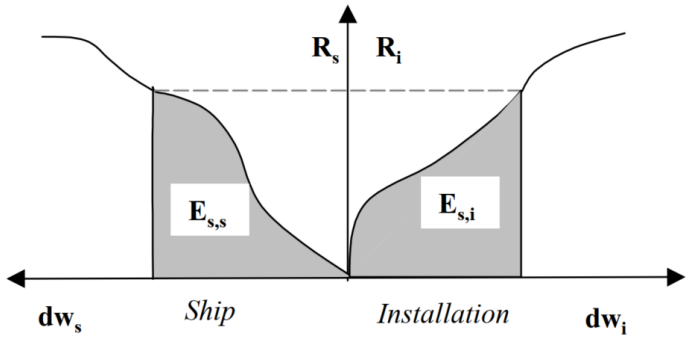

Figure 3.4: The strain energy dissipated equals the total area under the load-deformation curve(DNVGL-RP-C204, 2017).

The reaction force, R, on the ship and installation, must be the same according to Newton's Third Law, which states that "for every action, there is an equal and opposite reaction." The energy dissipation distribution of the structures depends on the resistance ratio, as seen in Figure 3.1. For ductile or strength design, the gray area would cover only one of the sides. The load level will in these cases, be much higher than for the shared-energy design shown in Figure 3.4.

Equation 3.23 describes this energy dissipation relation. When E_s is known, an incremental procedure can be solved since the load level for a given collision energy is not known in advance.

$$E_s = E_{s,s} + E_{s,i} = \int_0^{w_{s,max}} R_s dw_s + \int_0^{w_{i,max}} R_i dw_i \tag{3.23}$$

The load-deformation curve for a given collision can be found exactly by FE-analysis. This gives the most accurate results by performing a coupled simulation where the external dynamics are calculated simultaneously in the analysis. A load-deformation curve can also be obtained for decoupled analyses where the collision path is predetermined.

This method has limitations when the impact point differs from the ship center of gravity(COG) and for oblique collision angles. For some collision scenarios, there are general load-deformation curves that can be utilized as a first estimate. For example for an OSV, DNVGL-RP-C204 (2017) presents general load-deformation curves for bow, side and stern impact. In these curves, the struck column is assumed to be rigid; hence all deformation occurs in the ship. An example of one of these curves are presented in Figure 3.5, where the load-deformation curves for an ICE-1C class OSV and a regular OSV are shown. When the diameter of the column increases towards 10 meters, the results will converge towards a plane wall impact.

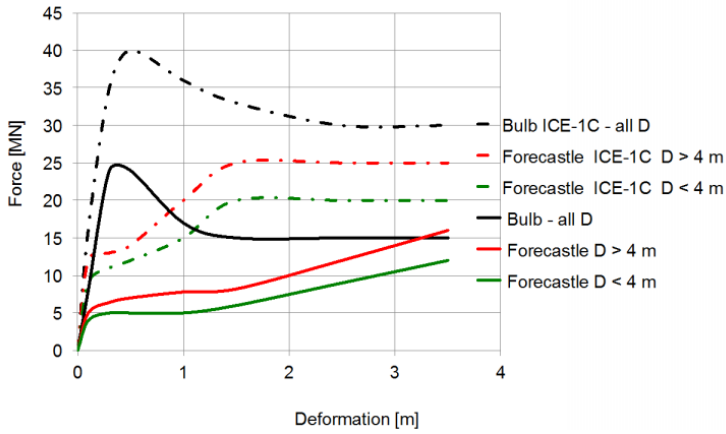

Figure 3.5: Force-deformation relationship for bow impacts from supply vessels with displacement 5-10.000 DWT - standard bulbous bow with no ice-reinforcement and ICE-1C class(DNVGL-RP-C204, 2017).

3.4 Equivalent displacement method

A ship structure does not have the same strength at all points. The bulb is, for example, stronger than the forecastle in most cases. Several decks, stiffeners, and cut-out positions also lead to a non-uniform strength over the ship surface. This means that the maximum deformation of the two structures can occur at different positions, and can not be compared easily. This can be seen in Figure 3.6, which is taken from one of the collision scenarios that will be discussed in this thesis. It can be seen that the maximum displacement for the bow occurs at the forecastle and the lower part of the FPSO ship-side. Therefore, it is useful to define a common displacement variable for both structures that is not dependent on the physical deformation of the structures. This variable is called equivalent displacement.

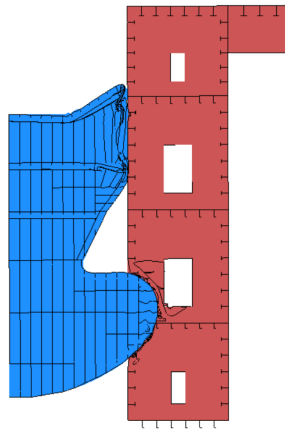

Figure 3.6: Deformation for head-on collision

In an FE-analysis, it is possible to obtain the dissipated energy. The dissipated energy is in Abaqus recorded as internal energy. It can be seen in Figure 3.7, that the internal energy is increasing for the entire duration of the collision. The figure also shows how the forecastle dissipates most of the energy before the bulb makes the first contact at 1.2 meters. After this point, the FPSO-side dissipates more of the energy, while the strong bulb dissipates very little energy. It is possible to obtain an expression for the equivalent displacement by utilizing the reaction force curve and the internal energy data. This can be obtained by using the trapezoidal rule for numerical integration to rewrite Equation 3.23, for example, for the ship:

$$E_{s,s} = \int_0^t R_s dw_s = \sum_{i=1}^{t} \frac{R_{s,t-1} + R_{s,t}}{2} dw_s \tag{3.24}$$

$$\Downarrow$$

$$dw_s = \sum_{i=1}^{t} \frac{\Delta E_{s,s}}{\frac{R_{s,t-1}+R_{s,t}}{2}} = \sum_{i=1}^{t} \frac{2(E_{s,s,t} - E_{s,s,t-1})}{R_{s,t-1} + R_{s,t}} \tag{3.25}$$

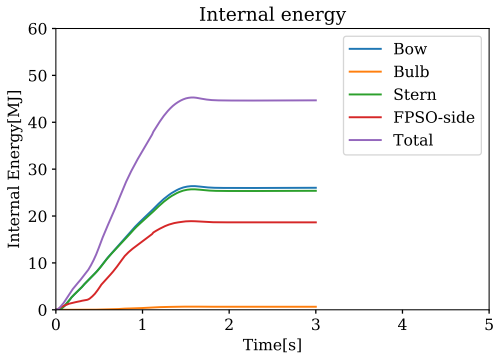

Figure 3.7: Internal energy dissipation for the collision scenario shown in Figure 3.6

The equivalent displacement variable makes it possible to plot load-deformation curves for OSV and FPSO, where the reaction force and the energy dissipation are consistent. This is a favorable way to visualize the energy dissipation for the two structures. It is worth noting that the effect of utilizing the equivalent displacement instead of manually choosing the real displacement depends on the relative strength of the structures. For structures with less complex strength distribution, the equivalent displacement will be closer to the real displacement.

3.5 Coupled approach

To integrate global motion and local damage, either a coupled or decoupled approach can be used. A coupled approach is more precise, as it describes the collision process with the correct motions of both involved structures in parallel. No initial assumptions for the penetration path are needed for this approach. The structure motions do not correspond in the decoupled approach, a method based on the conservation of momentum. A comparison of the two methods has been performed by Tabri (2012) and indicates that the collision deformation energy is predicted with satisfying accuracy.

On the other hand, the penetration path has a notable difference between the coupled and decoupled approach. For the decoupled approach, the accuracy is dependent on the collision symmetry. Reasonable results can be achieved for symmetric collisions. However, very few collisions are fully symmetric for different reasons(Lützen et al., 2000). For example, since the contact point usually is not midships, the struck ship may have an initial velocity or that the collision angle is not a right angle.

The effect of the fluid is quite complex to include in a finite-element code. A simplified coupled method was therefore proposed by Pill and Tabri (2011), where buoyancy, and

restoring forces were neglected. This can be a reasonable assumption since the impact period in a ship collision is small compared to the natural periods of a ship. The radiation forces are simplified to constant added mass terms. This method resulted in good agreements with experimental results. Nevertheless, for more complex ship motions, this method can have limitations.

A fully coupled model that captures transient hydrodynamic effects was proposed by Yu and Amdahl (2016). This model can be used in the FE-software LS-Dyna without any external routines needed and is, therefore, more efficient than pre-existing coupled models. The results from this method show that the decoupled and simplified coupled methods fail to capture secondary impacts that origins from the periodic ship motions. For some collision scenarios, this effect can make the simplified models unconservative.

4 Theory of Finite Element Analysis

The Finite Element Method(FEM) is an approximate numerical analysis method for solving problems described by partial differential equations(PDE). These PDEs are very difficult or not possible to solve analytically for the majority of physical problems. To solve the problem, the structure is discretized into smaller parts called finite elements. Each element is described by a set of equations, which for structural problems, has the displacement as the unknown variable. For a small element, it is assumed that the difference in displacement is small enough to be interpolated from the nodes at the boundary of the element. For a linear analysis, it is also assumed that the material is linear and elastic. The equation can, with these assumptions be solved, and then be assembled into a global system of equations that describes the whole structure. FEA can be used to solve many different engineering problems such, such as:

- Structural mechanics
- Machine design
- Acoustics
- Electromagnetism

The accuracy of FEM depends on many factors. One factor is the element size, also called the mesh size. Smaller elements will give a more accurate solution since the interpolation intervals over the elements will be shorter. However, more elements in total can increase computational time dramatically. Therefore, it may be essential to perform a mesh sensitivity test to find a proper balance between accuracy and computation time. Another important accuracy factor is the choice of element types. The element types determine the equations that have to be solved for each element. Different properties of the elements make it important to choose appropriate types to get accurate results, while not using too much calculation power. For example, can a truss element with only translational DOFs be the right choice for a truss-work, but not appropriate for an element with lateral loading.

The system of equations for a linear structural FEA can be written:

$$\mathbf{Kr} = \mathbf{R} \tag{4.1}$$

K is the global stiffness matrix and is an assembly of the local stiffness matrices for all elements. This depends on the material parameters, boundary conditions, and element

type. The assembly is done by summing all stiffness components from different elements that apply to one specific node. The total stiffness for each node is then placed in the global stiffness matrix. The nodal displacement vector **r**, is the variable that the equation is solved for. This variable can then be used to find stresses and strains at each node.**R** is the vector describing the forces acting on each node. Equation 4.1 can be solved in two different ways. For smaller problems, or when the bandwidth of the stiffness matrix is much smaller than the number of DOFs, a direct solution is the best choice. This is performed by a type of Gaussian elimination. For structures with many DOFs, an iterative solver may be more efficient (Kiendl, 2018).

4.1 Non-linear FEA

For structures subjected to accidental loads, there are usually involved large deformations and inelastic stresses and strains beyond the elastic limit. A linear elastic analysis is, therefore, not suitable for ALS analysis. The structural integrity check should instead be done by a non-linear FEA or with the use of simplified plastic methods (DNVGL-RP-C204, 2017). Three important nonlinearities need to be taken into account, geometrical, material, and boundary nonlinearities.

4.1.1 Geometric nonlinearity

The change of geometry from large displacements changes the stiffness of the elements. This can be exampled by the two-bar problem, which is shown in Figure 4.1. The two-bar problem consists of two bars supported and connected by pin-joints. The bars are initially orientated by an upwards angle α_0, with a final angle, α, depending on the displacement, r. A point load, R, is acting on the point connecting the two bars.

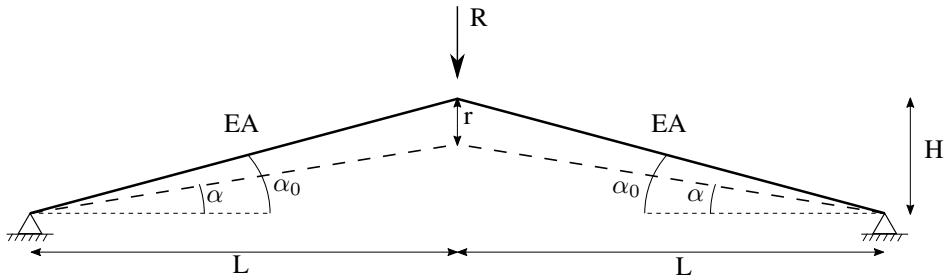

Figure 4.1: Two-bar problem. Figure based on Figure 12.2 in Moan (2003).

The axial shortening of the bars can be expressed as:

$$\Delta = \frac{L}{cos\alpha_0} - \frac{L}{cos\alpha}. \tag{4.2}$$

which gives a strain of

$$\epsilon = \frac{\Delta}{L/cos\alpha_0} = 1 - \frac{cos\alpha_0}{cos\alpha}. \tag{4.3}$$

The equilibrium equation then becomes

$$R = 2Ssin\alpha = 2EAsin\alpha \left(1 - \frac{cos\alpha_0}{cos\alpha}\right). \tag{4.4}$$

By substituting the trigonometric functions with the variables in the figure, for example $cos\alpha_0 = \frac{L}{\sqrt{L^2+H^2}}$, and assuming small α and α_0, the non-linear equilibrium equation can be seen in Equation 4.5. A more thoroughly derivation can be found in Moan (2003).

$$R = \underbrace{\frac{2EA}{L}\alpha_0^2 \left(1 - \frac{r}{h}\right)\left(1 - \frac{r}{2H}\right)}_{K(r)} r \tag{4.5}$$

or for a general system of equations

$$\mathbf{K}(\mathbf{r})\mathbf{r} = \mathbf{R}. \tag{4.6}$$

K(r) can be divided in a linear term, K_0, and a nonlinear geometric term, K_g, by writing out Equation 4.5

$$K(r) = \underbrace{\frac{2EA}{L}\alpha_0^2}_{K_0} + \underbrace{\frac{EA}{L}\alpha_0^2 \left(\frac{r}{H} - 3\right)\frac{r}{H}}_{K_G}. \tag{4.7}$$

This relation is shown in Figure 4.2. For small displacements, it can be seen that the linear theory can be applied. At the first maxima of the non-linear curve, a phenomenon called snap-through will occur. This means that the solution will jump to the next stable equilibrium condition, which is pointed to in the Figure by the dashed line.

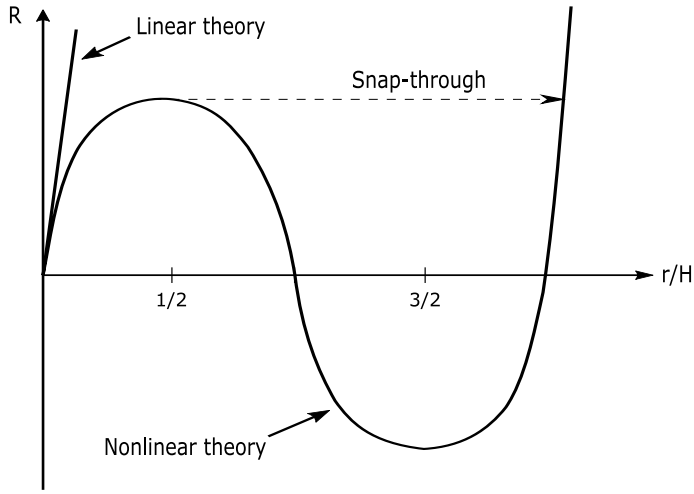

Figure 4.2: Load-deflection curve for two-bar problem(Moan, 2003).

As seen in Figure 4.2, reducing r/H results in a decrease in the geometric stiffness. The reason for this is that the compression component in the bars will be smaller for smaller angles. This means that more of the force will result in displacement. The snap-through phenomena involve quick and large displacements and can be complicated when performing numerical integration, e.g., in an FE analysis. Overall, this example shows the big contribution of the non-linear geometric stiffness to the total stiffness of the structure, especially when large displacements occur.

4.1.2 Non-linear material behavior

In problems involving material nonlinearity, the stress-strain relationship is a non-linear function of stress, strain, and time (Moan, 2003). These material properties can be challenging to obtain, in opposite to the linear-elastic material properties. Therefore additional material testing may be needed.

An example of non-linear material behavior is shown in Figure 4.3 for a typical mild steel. Here it can be seen that the linear elastic behavior only applies below the proportionality limit, σ_P. The plastic strain starts after this level and is extensive for mild steel, which has a plateau in the perfect plastic region. Many materials, including steel, can exhibit strain hardening. This can be seen in the Figure, where the stress level increases after the plateau. This is an important property to take into regard for non-linear analy-

sis. If the stress in the material is removed, a residual plastic strain, ϵ_P remains if plastic strain has occurred during loading.

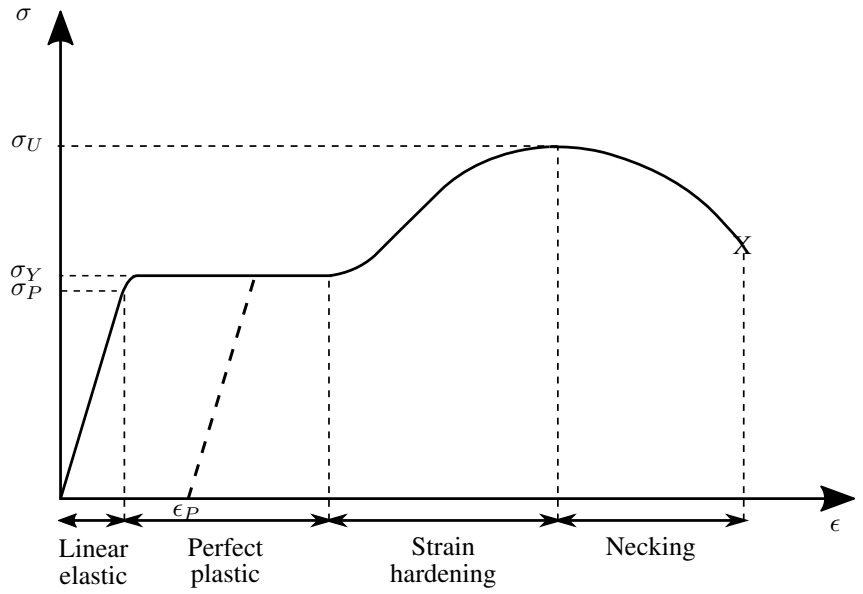

Figure 4.3: Stress-strain curve for a typical mild steel. Figure based on Figure 12.17 in Moan (2003).

According to Moan (2003), the elasto-plastic behavior of metals in a multidimensional stress state is characterized by three different rules, the *yield criterion*, a *hardening rule*, and a *flow rule*.

The *yield criterion* defines when the plastic strains are generated. For steel material, it is common to utilize the von Mises yield criterion presented in Equation 4.8. The subscripts 1, 2, and 3 represent the x, y, and z-axis, respectively, and τ represents shear stress. The yield criterion will change depending on the plastic strain history.

$$\sigma_v = \frac{1}{\sqrt{2}}\sqrt{(\sigma_{11}-\sigma_{22})^2+(\sigma_{22}-\sigma_{33})^2+(\sigma_{33}-\sigma_{11})^2+6(\tau_{12}^2+\tau_{23}^2+\tau_{31}^2)} \quad (4.8)$$

The *hardening rule* describes the effect of the history of plastic flow on the yield criterion. This can be illustrated by an example shown in Figure 4.4. From origo to point A, there is only elastic strain as the stress is below yield. From point A to B, the loading is

above yield, and the material has experienced plastic strain. However, it can be seen that the tangent modulus $E_t > 0$, which means that the material develops increased yield capacity. This can be shown by unloading the material to point C, where the strain follows the elastic modulus, E by definition. If the material is reloaded from point C, the response will be elastic for $\sigma < \sigma_B$. Hence the material has hardened.

If a reversed loading(compression) is applied to the hardened material, the strain will follow the curve from point C to D. If the yielding in compression is assumed to be occurring at $|\sigma| = \sigma_B$, the hardening is defined to be *isotropic*. However, this is usually not the case for common structural metals. For these materials, a typical behavior is a yield in compression at approximately $\sigma_B - 2\sigma_Y$ according to Moan (2003). Therefore, the *kinematic* hardening rule is introduced to represent the real material behavior better. For this rule, the elastic range $2\sigma_Y$ is always applicable, as seen in Figure 4.4.

The hardening is assumed to follow a Hollomon-type hardening rule. In general, this relation can be expressed as

$$\sigma_y = K\varepsilon_p^n \tag{4.9}$$

where K is the material strength coefficient and n is the strain hardening exponent. To account for a yield plateau, which is typical for mild steels, the hardening rule can be extended to

$$\sigma_y = K\Big[\big(\frac{\sigma_0}{K}\big)^{\frac{1}{n}} + \varepsilon_p - \varepsilon_{plateau}\Big]^n \quad if \quad \varepsilon_p > \varepsilon_{plateau}. \tag{4.10}$$

The strain hardening will, in this expression, start after the yield plateau, $\varepsilon_{plateau}$.

The *flow rule* describes the relation between the stress increments $d\boldsymbol{\sigma}$ and strain increments $d\boldsymbol{\varepsilon}$ for multidimensional problems(Moan, 2003). For a uni-axial problem the flow rule can be described as $d\sigma = E_t d\varepsilon$, where $E_t = E$ in the elastic region.

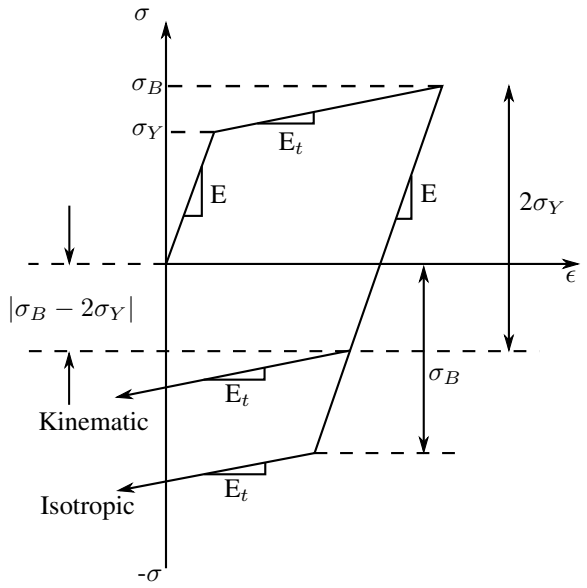

Figure 4.4: Stress-strain curve showing kinematic and isotropic hardening. Figure based on Figure 12.17 in Moan (2003).

4.1.3 Boundary conditions

Non-linear boundary conditions are common in contact problems, e.g., for ship collisions. A simple example of this is shown in Figure 4.5, where there is no displacement after the cantilever touches the support.

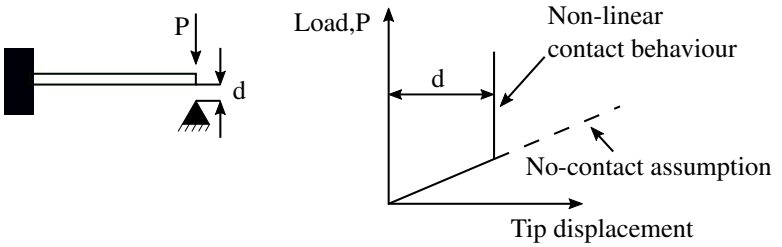

Figure 4.5: Non-linear boundary condition(Moan, 2003).

4.2 Fracture models

A precise definition of failure is vital for all FE analyses. The tensile failure mode is important for collision analyses where high deformations occur. Buckling failure is also important, while, for example, fatigue does not play an important role. Multiple fracture criteria are commonly used today. Three of these are presented in the following paragraphs.

When visualizing material limits, it is common to use a forming limit diagram(FLD). This diagram has the principal strains of the material. ε_1 and ε_2, plotted in the FLD at the initial plastic instability. The instability points are obtained from experiments. The region above the curve is the zone where the material fails. The FLD is only valid for proportional strain rates which can be expressed as $\beta = \dot{\varepsilon_2}/\dot{\varepsilon_1}$, where $\dot{\varepsilon_i}$ is the strain rate and the strain rate ratio, β, is constant at all times. According to Alsos et al. (2008), the assumption of constant β is not automatically true for large deformation cases, for example ship collisions. The reasons for this are, among others, material hardening and changed geometry. An alternative to strain-based FLD is the stress-based FLD, which was first presented by Arrieux et al. (1982). The advantage of using the stress-based approach, according to Alsos et al. (2008), is that the strain-based criteria remain relatively unchanged for strain rate development and that it is more convenient to implement in a finite element analysis. An example of an FLD for both strain-based and stress-based approach is shown in Figure 4.6.

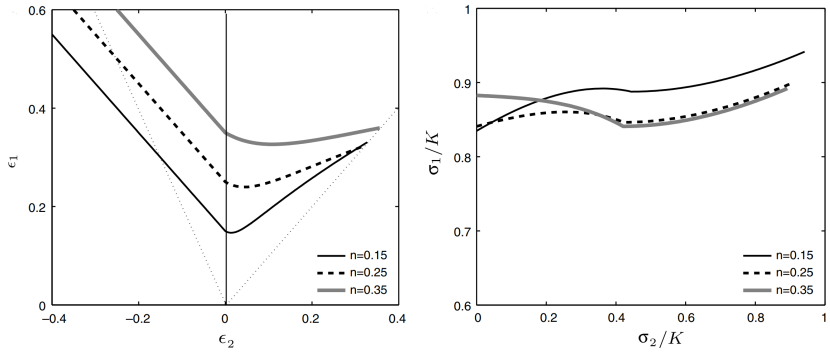

(a) Strain based FLD.

(b) Stress based FLD.

Figure 4.6: FLD for strain and stress based method. Both figures illustrate the same material and fracture model. The figure is obtained from Alsos et al. (2008).

4.2.1 BWH criterion

The Bressan-Williams-Hill(BWH) instability criterion is a combination of Hill (1952) local necking criterion and Bressan and Williams (1983) shear instability criterion. This criterion utilizes a stress-based forming limit approach. The Hill (1952) criteria is only valid in the negative β range, while the Bressan and Williams (1983) criteria is valid for all strain rates. However, the accuracy of the latter is reduced for negative β values, which is why the two criteria are combined to the BWH-criterion, as seen in Equation 4.11. The full derivation of this criterion can be found in Alsos et al. (2008). The BWH-criterion can be implemented in the FE-software Abaqus Explicit by a VUMAT, a user-defined material subroutine.

$$\sigma_1 = \begin{cases} \frac{2K}{\sqrt{3}} \frac{1+\frac{1}{2}\beta}{\sqrt{\beta^2+\beta+1}} \left(\frac{2}{\sqrt{3}} \frac{\hat{\varepsilon}_1}{1+\beta} \sqrt{\beta^2+\beta+1} \right)^n, & \text{if } \beta \leq 0 \\ \frac{2}{\sqrt{3}} K \frac{\left(\frac{2\hat{\varepsilon}_1}{\sqrt{3}}\right)^n}{\sqrt{1-\left(\frac{\beta}{(2+\beta)}\right)^2}}, & \text{otherwise} \end{cases} \tag{4.11}$$

Where K and n are parameters describing the hardening behavior of the material, σ_1 is the major principal stress, and $\hat{\varepsilon}_1$ is the critical strain. This can be assumed to be equal to n if no other information is available. The BWH-criteria is found to correspond well to experimental data according to Alsos et al. (2008). This can also be seen in Figure 4.7 retrieved from Storheim et al. (2018).

4.2.2 RP-C208 criterion

A simplified tensile failure criteria is presented in DNVGL-RP-C208 (2016). For this criterion, failure is assumed when the maximum principal strain, ε_{crl} is exceeded. This can be calculated as

$$\varepsilon_{crl} = \varepsilon_{crg}\Big(1 + \frac{5t}{3l}\Big), \tag{4.12}$$

where ε_{crg} is a global strain calculated from a calibration case. For mean S235 steel, $\varepsilon_{crg} = \delta_x / L_{calibration} = 80/450 = 0.18$. The length thickness of the element is described t and l, respectively. This criterion results in less than 50% strain energy dissipation compared to the GL fracture criterion(Storheim et al., 2018). This may imply that the RP-C208 criteria can be inaccurate. For situations where low capacity is governing, it will be very conservative, and for mean capacity, as for striking ships, it can be unconservative. This can be seen in Figure 4.7.

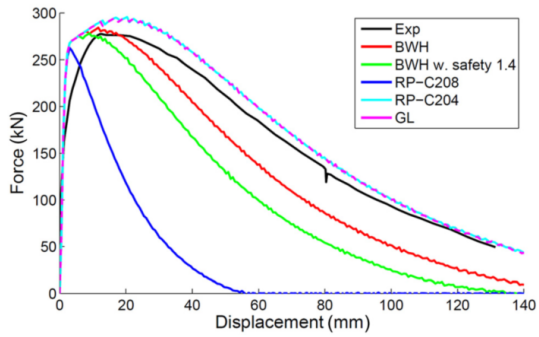

Figure 4.7: Force-Displacement curve comparison for experiment from Simonsen and Törnqvist (2004) and different fracture criteria. Figure retrieved from Storheim et al. (2018).

4.2.3 RTCL criterion

Törnqvist et al. (2003) proposed a fracture model named RTCL, which is a combination of Rice-Tracey(RT) and Cockcroft-Latham(CL) criteria. According to Törnqvist et al. (2003), the CL criterion is believed to predict ductile shear fracture correctly, and RT is suitable for predicting void growth. In Figure 4.8, both criteria are shown as well as the RTCL criteria. The RTCL criterion is fully derived in Törnqvist et al. (2003).

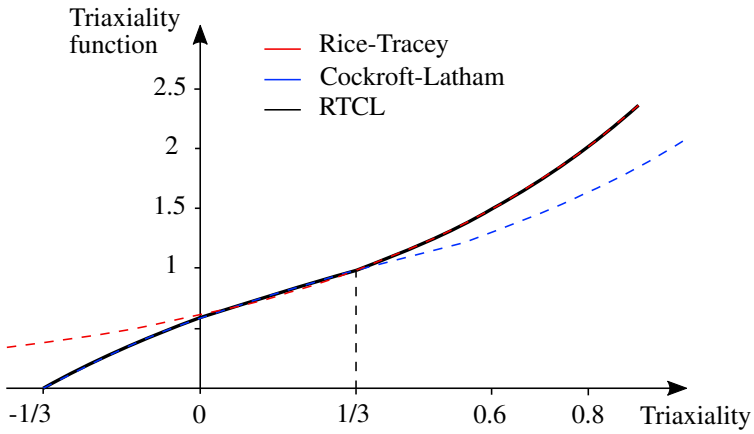

Figure 4.8: Triaxiality functions for RT, CL and RTCL. Figure is based on Figure 2.5 in Törnqvist et al. (2003).

4.3 Analysis method

The general dynamic equilibrium equation can be seen in Equation 4.13 and describes the relation between external excitation forces, $\mathbf{F_{ext}}$, and inertia, damping and stiffness forces. This is an extension of the static equilibrium equation, where the mass and damping terms are neglected. To be able to analyze a dynamic problem in the time-domain, the dynamic equilibrium equation needs to be solved.

$$\mathbf{M}\ddot{\mathbf{u}}(t) + \mathbf{C}\dot{\mathbf{u}}(t) + \mathbf{K}\mathbf{u}(t) = \mathbf{F_{ext}}(t) \tag{4.13}$$

M is the mass matrix of the system, including added mass, **C** is the damping matrix, and **K** is the stiffness matrix. The displacement vector, **u**, is the variable that needs to be solved. For non-linear problems, there exist no analytical solutions, which means numerical methods is utilized., Either *implicit* or *explicit* methods can be utilized to obtain numerical approximations of the solution.

For the explicit methods the equation system is evaluated at the old time-step t_n, while the implicit methods evaluate the equation system at the new time-step t_{n+1}(LS-Dyna, 2020). In the implicit analysis, the matrices in the set of non-linear equilibrium equations must be inverted and then solved at each time-increment. This means that the computation time rises very fast for large problems. A positive factor is that the implicit method is unconditionally stable, which means that there are no restrictions on the time-step. In this thesis, an explicit solving method will be used, and implicit methods will not be discussed further.

4.3.1 Explicit solver

Explicit solvers are suitable for large equation systems in dynamic analyses. The explicit solver requires less computational effort for each time-step compared to the implicit method. The reason for this is that the explicit solver does not require matrix inversion and iterations. However, the explicit method is only stable for sufficiently small time-steps, contrary to the implicit method.

The equations of motion for the structure are integrated into Abaqus Explicit using the central-difference integration rule and the use of diagonal element mass matrices (Abaqus, 2020). The central difference integration rule is shown in Equation 4.14.

$$\begin{aligned} \dot{\mathbf{u}}^{(i+\frac{1}{2})} &= \dot{\mathbf{u}}^{(i+\frac{1}{2})} + \frac{\Delta t^{(i+1)} + \Delta t^{(i)}}{2}\ddot{\mathbf{u}}^{(i)} \\ \mathbf{u}^{(i+1)} &= \mathbf{u}^{(i)} + \Delta t^{(i+1)}\dot{\mathbf{u}}^{(i+\frac{1}{2})} \end{aligned} \tag{4.14}$$

In this equation, $\ddot{\mathbf{u}}$ is acceleration and $\dot{\mathbf{u}}$ is velocity. The superscripts determine the increment number of the vector, as seen in Figure 4.9. The reason for the computational efficiency comes from the lumped mass assumption. This means that it is no need for complex mass matrix inversions.

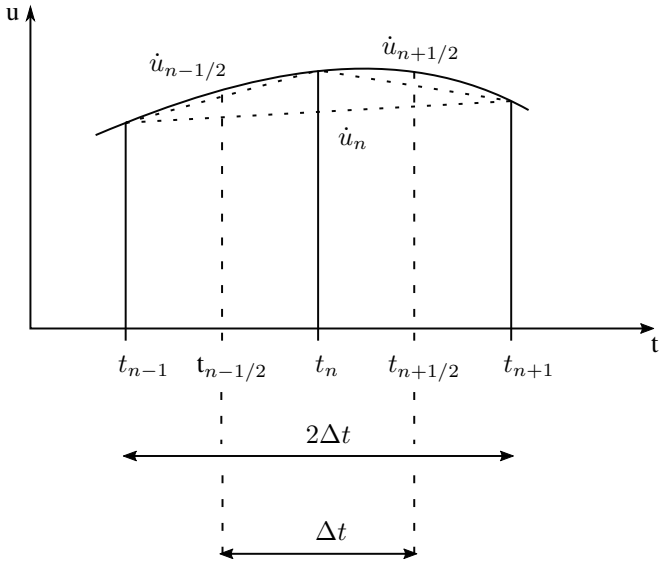

Figure 4.9: Central difference method.

The central difference method is conditionally stable, which means that a sufficiently small time-step has to be chosen. A conservative estimate of the required time-step is given in DNVGL-RP-C204 (2017) as

$$\Delta t = L_s \sqrt{\frac{\rho}{E}}, \tag{4.15}$$

where L_s is the characteristic element size of the smallest element, ρ is the material density, and E is the material modulus of elasticity. This equation gives very small time-steps, which makes the explicit solver suitable for shorter time-spans, for instance, in impact response analysis. In Abaqus Explicit, the stability time-step limit is automatically determined as

$$\Delta t \leq \frac{2}{\omega_{max}}(\sqrt{1+\xi^2} - \xi), \tag{4.16}$$

where ω_{max} is the highest eigenvalue in the system, and ξ is a small amount of damping introduced to control high-frequency oscillations.

5 Finite element models and analysis set-up

The finite element model in this thesis consists of a pre-existing OSV-bow model and an FPSO-side model that is made for this thesis specifically. In this Chapter, the modeling of both structures, boundary conditions, and collision scenarios will be discussed. There is also conducted some sensitivity and validation analysis, which will also be presented.

The element used for both FE-models is a general-purpose 4-node shell element with reduced integration and finite membrane strains named *S4R* in Abaqus. Shell elements are suitable when one dimension is significantly smaller than the two other dimensions, which is the case for the plating and the stiffeners. There are used five through-thickness integration points to allow non-linear behavior in the shell.

The contact property in Abaqus is used to define the mechanical surface interaction model that governs the behavior of the surfaces when in contact. For this analysis, a penalty friction formulation with a friction coefficient of 0.3 is used as contact property. In addition, default properties still apply, for example, no thermal interaction.

5.1 OSV-bow model

The pre-existing bow-model is based on a modern 7500-displacement offshore supply vessel(OSV). The plate thickness varies from 7 millimeters in the top-deck to 12.5 millimeters in the bulb outer plating. The element size is approximately 120 millimeters, and the stiffener spacing is varying between 600 and 750 millimeters. The bow model consists of 67872 elements, where 99.7% is quad-elements, and the remaining is triangular elements. The principal dimensions of the ship are presented in Table 5.1, and the dimensions for the bow can be seen in Figure 5.1.

Table 5.1: Main dimensions of striking OSV

Length B.P.	Width	Depth	Draft	Δ
78.8m	18.8m	7.6m	6.2m	7500tons

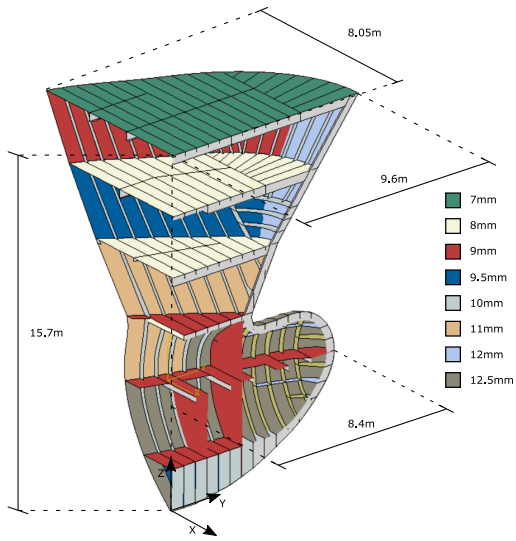

Figure 5.1: Dimensions of the OSV-bow used in the analysis

5.1.1 Boundary conditions

All nodes at the back of the bow are subjected to a kinematic coupling constraint to the COG of the ship. This constraint simulates a rigid hull girder from the COG to the back of the bow, by defining the distance and rotation between each node and the COG constant. This makes it possible to include the rigid-body motions of the ship. The COG of the ship is assumed to be located in (x,y,z)=(39.4m,0m,5m), when the origin is defined to be at the rear perpendicular. According to Pedersen and Li (2009), the elastic energy absorbed by the hull girder in a collision is between 1% and 6% of the collision energy. This makes it reasonable to assume a rigid hull girder for this thesis.

The COG is fixed in all directions except the impact direction when rigid body motions are not included. When rigid body motions are included, only the z-direction is fixed. The analysis would be more accurate if this boundary condition were substituted with a spring to ground option simulating the heave restoring force. However, this is yet to be a feature in Abaqus Explicit and, therefore not used. Because of the short period of a collision impact, the roll and pitch DOFs are free to move. A spring option could have increased the accuracy of these DOFs as well.

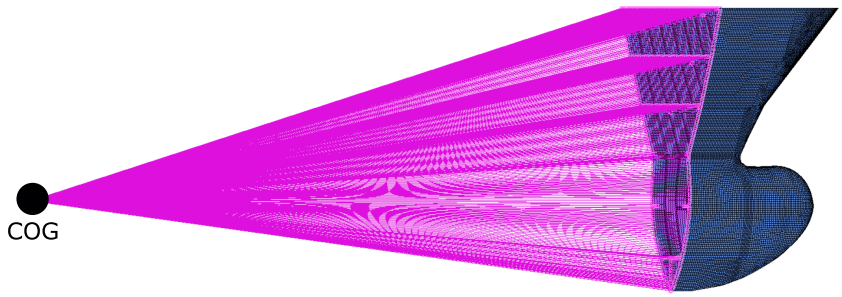

Figure 5.2: Kinematic coupling constraint shown in purple. All nodes on the back of the bulb is constrained to the COG.

The constant added mass factors and radii of gyration are calculated by utilizing the expressions derived by Popov et al. (1969), which can be found in Appendix A. The resulting mass and inertia properties are presented in Table 5.2. The factors are implemented by utilizing the inertia feature in Abaqus and connected the property to the COG. It is important to note that the striking bow coordinate system has the y-axis defined as alongships, as seen in Figure 5.1. This means that, for example, the roll direction is rotation about the y-axis. The reason for this is the collision base case of the bow hitting the FPSO-side with a 90-degree angle. The FPSO side is the most massive object and is decided to use the conventional coordinate system with the x-axis along the ship length.

Table 5.2: Inertia properties of the striking bow. M_{ii} is mass and added mass, and I_{ii} is moment of inertia including added mass.

M_{11}[kg]	M_{22}[kg]	M_{33}[kg]	I_{11} [kg· m^2]	I_{22}[kg· m^2]	I_{33}[kg· m^2]
12.45E6	8.25E6	15.39E6	6.23E9	0.31E9	4.39E9

The contribution from the modeled bow is neglected, as the influence on the inertia is less than 3%, as seen in Table 5.3.

Table 5.3: Modeled bow influence on inertia

Contribution on inertia			Ratio of total
M	66.5E3	[kg]	0.9%
I_{11}	119.2E6	[kg· m^2]	1.9%
I_{22}	3.5E6	[kg· m^2]	1.1%
I_{33}	116.7E6	[kg· m^2]	2.7%

A predefined velocity field is defined at the initial step for all analyses. This is applied for all nodes on the striking bow and the inertia element at the ship COG. The velocity component in the x- and y-direction is corresponding to the impact angle of the bow. The reason for selecting all nodes is to remove the effect of accelerating the elements, which can cause stresses from inertia effects. For coupled analysis, there are no defined velocities during the impact. For the decoupled analysis, however, a constant velocity in the impact direction is applied at the ship COG. The assumption of a decoupled penetration path equal to the initial impact direction is a reasonable assumption, according to Zhang (1999).

5.1.2 Ice-reinforced OSV-bow

The ICE 1-C class OSV-bow used in the analyses is shown in Figure 5.3. It can be seen that the plate thickness is significantly higher since it is ice-reinforced than the standard bow shown in Figure 5.1. The majority of the outer plate of the ice-strengthened bow is 15mm and 17mm, while the standard bow has plate thickness varying between 9mm and 12.5mm. In addition to this, most of the other dimensions are also increased for the ice-strengthened bow. It can also be seen that the geometry is a little different. There is, for example, a vertical plate of high thickness at the top part of the forecastle, and the bulb is more slender than the standard bulb.

All other properties of the ship are assumed to be identical to the standard bow, i.e., principal dimensions, mass, and inertia properties. This was assumed to make it possible to make reasonable comparisons. The principal dimensions of the ice-bow are about 15% larger than the standard bow, which means that it is likely that the corresponding ice-reinforced hull structure is a little bigger in reality than what is assumed for this thesis. The boundary conditions are also equal to the standard bow.

The bow model consists of 123804 elements, with 99.8% being quad-elements, and the remaining are triangular elements. The element size is for most of the structure of about 120mm. The stiffener spacing is about half of the standard bow, and the stiffener lengths are shorter as well. There are also more frames for the ice-strengthened bow.

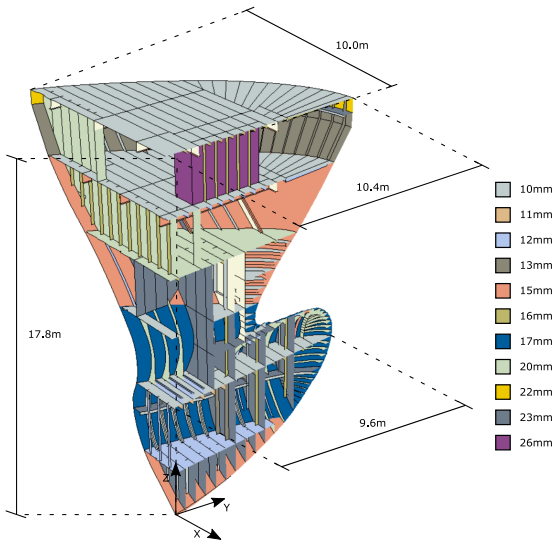

Figure 5.3: Dimensions of the ice-reinforced OSV-bow used in the analysis

5.2 FPSO-side model

An FE-model of the FPSO-side is established in the modeling software Patran. The dimensions are based on a typical North Sea FPSO and are presented in Table 5.4.

Table 5.4: Main dimensions of FPSO

Length B.P.	Width	Depth	Draft	C_b	Δ
295m	58m	31m	24m	0.85	357 tons

The frame-spacing of the FPSO-side is 800mm, with a web frame spacing of 4000mm. The middle tank of the FPSO is the one subjected to the collision in this thesis. This tank is 36 meters long, which implies 45 frames. The impact between FPSO and the OSV will occur at the middle of the tank between frames 170 and 175. This is the most critical impact position for the tank because it is furthest away from the transverse bulkheads. To have sufficient boundary condition accuracy and reducing computational cost, frame 160 to 190 is modeled. This can be seen in Figure 5.4, where the ship is viewed from the side.

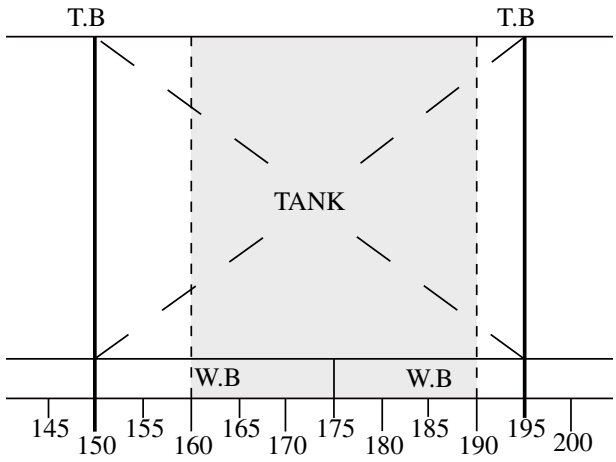

Figure 5.4: Illustration of frame spacing of FPSO-side. T.B shows transverse bulkheads, W.B is water ballast tank and the gray area illustrates what frames are modeled in Patran.

The dimensions of the FPSO is much larger than the OSV. Since the OSV maximum draft is 6.2 meters, the impact location on the FPSO will most likely occur at the top half of the ship. The ship-side is therefore modeled without the bottom 8 meters of the FPSO. Because of the strong longitudinal bulkhead at 9 meters from the centerline, it is not important to model the center-most part of the ship. This is illustrated in Figure 5.5, where a simplified mid-ship drawing is shown. The modeled part of the FPSO is marked in red color.

A collision between an FPSO in ballast condition and a maximum loaded OSV defines the lowest possible impact point on the FPSO. For this condition, it may be needed to model more of the lower part of the FPSO. However, this should not be included for most of the collision scenarios, as this will increase the computation cost, with minimally improved accuracy.

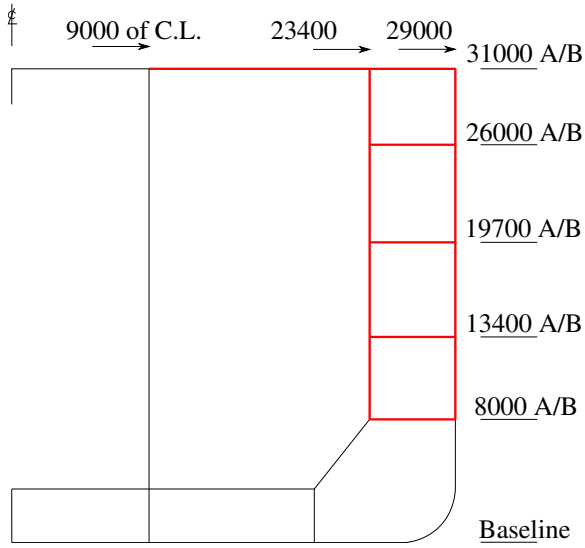

Figure 5.5: Illustration of mid-ship drawing.

The FPSO-side model consists of 483872 elements, where all are quadrilateral elements. The element size is decided to be 100mm. This element size is chosen based on the common practice for such models, stiffener spacing and height, and computational cost. A mesh size of 100mm makes four elements for the stiffener web, height, and at least one element for each flange, which can be seen in Figure 5.6a. There are some minor configurations to the stiffener spacing, web height, and cut-out size compared to the real drawings. This is done to make all parts of the structure correspond well to the element size. The stiffener spacing is for most of the model 900mm, and most of the stiffeners are 400x200 T-profiles. All stiffener flanges are free to move through all web-frames. This is done by excluding the nodes on the flanges when equivalencing the nodes in Patran. An illustration showing the free edges of the model can be seen in Appendix F.1.

The plate thickness of the FPSO-side is shown in Figure 5.6b. The model in the picture is cut between the web frames at frame 170 and 175 to show the interior of the model where the cut-outs and stiffener configuration can be seen. A mesh size of 150mm was utilized early in the modeling but resulted in a too irregular mesh and continuity problems because of varying stiffener spacing and cut-out size. A smaller mesh would have dramatically increased the computational cost of the analysis.

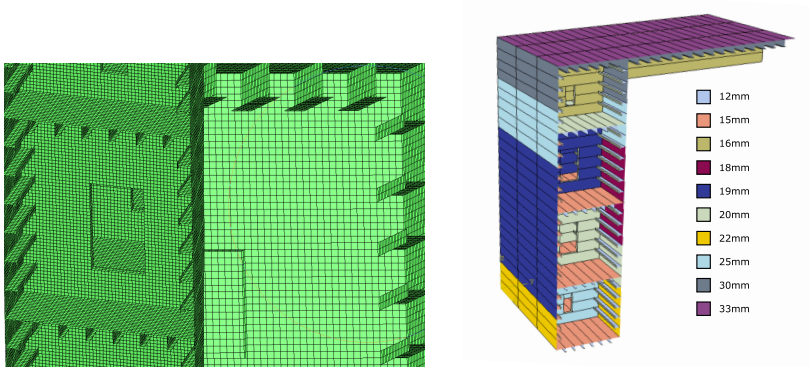

(a) FPSO mesh. Element size = 100mm (b) Plate thickness

Figure 5.6: FPSO model mesh pattern and thickness.

5.2.1 Boundary conditions

The modeling simplifications described in Section 5.2 leads to several assumptions to decide the boundary conditions. The edges of the model are, in reality, connected to the rest pf the FPSO hull-structure. It is important to model these connections as correct as possible, while at the same time not over-constraining the model. A sensitivity study for the DOFs that is not easy to define is presented in Figure 5.8. This is done to get a quantitative result of the eventual error margins for the boundary conditions.

The continuing longitudinal bulkhead at 9000 mm of the center and the inner and outer side-plating of the FPSO side constrain the model in direction 1 and rotation 5. This is shown in red, orange, and purple color in Figure 5.7, where the coordinate system used also can be found. The hopper tank below the model will give bottom support in direction 2 and direction 3 shown in dark blue. The bottom side, shown in light blue and dark blue in the figure, was by mistake constrained in direction 6. All analyses in this thesis are run with this constraint. The effect of this is shown to be neglectable by inspecting *BC1* and *BC2* in the sensitivity study, where this constraint is removed for the inner and outer sides, respectively. The transverse bulkheads at frame 150 and 195 in Figure 5.4 will contribute to support in rotation 4. The effect of removing this constraint is shown as *BC3* in the sensitivity study.

The bulkheads will also contribute to support in 2-direction. Because the model is only modeled between frame 160 and 190, this may make the analysis non-conservative and is therefore not opted for. The transverse bulkheads do also contribute to stiffness in rotation 6, which is fixed in this analysis. It is assumed that this has a neglectable impact on the final result, which is shown as *BC4* in the sensitivity study. Fixing the purple side

in direction 3 and rotation 6 is reasonable because of the strong longitudinal bulkhead. In general, it can be seen that the boundary conditions that are not clear, do not have a significant impact on the result. The small mistake for the bottom sides, does not have an influence either, which is why the analyses were not run one more time. The contour plots, showing the stress consecrations during the impact, does not show any stress concentrations at the boundaries. If this had been the case, the model might have been extended in some directions. Examples of these contour plots can be found in Section 6.1.

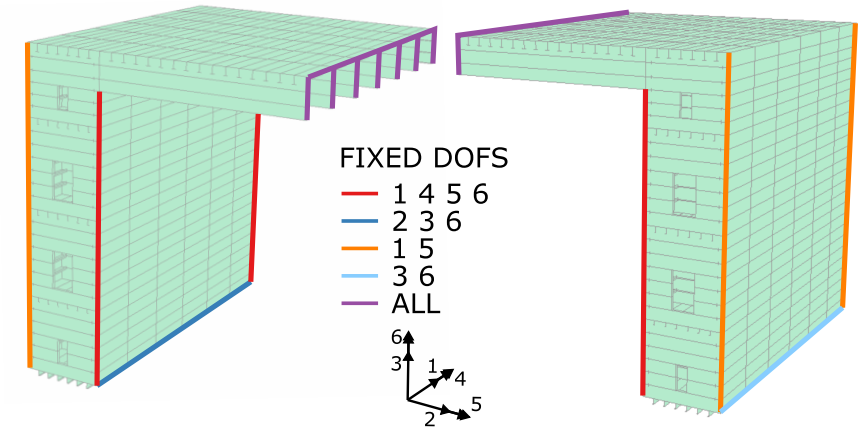

Figure 5.7: Boundary conditions for FPSO-model

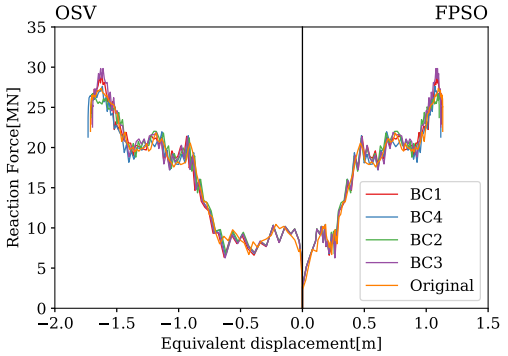

Figure 5.8: Sensitivity analysis for FPSO boundary conditions.

5.3 Material model

The two OSV-bows is in this analysis assumed to be built of mild steel of type NS A(S235). The FPSO-side consists of NS A steel below 26000mm above baseline, as shown in Figure 5.10. At the top part of the model, HS A, high tensile steel with a yield strength of 315MPa, is used. The OSV material is further assumed to have the mean material properties, and the struck FPSO is assumed to have a 5% low fractile resistance material. This is found to be reasonable assumptions for the ALS-condition where the target exceedance probability is 10^{-4}. For example, a high percentile material for the striking ship would result in a too low annual load probability(Storheim et al., 2018). The material data is shown in Table 5.5. Figure 5.10 show where the different steel-materials are used.

Table 5.5: Steel properties according to DNVGL-RP-C208 (2016)

	ρ $[kg/m^3]$	E $[GPa]$	ν $[-]$	σ_0 $[MPa]$	$\varepsilon_{plateau}$ $[-]$	K $[MPa]$	n $[-]$
S235 5%	7850	210	0.3	233	0.02	520	0.166
S235 50%	7850	210	0.3	315	0.02	700	0.166
S315 5%	7850	210	0.3	315	0.016	690	0.166

The stress-strain curve is then determined based on DNVGL-RP-C208 (2016) as a combination of a step-wise linear and a power-law with a yield plateau. In this analysis, the step-wise linear part is simplified to a linear plateau since the difference is minimal. The power-law is shown in Equation 5.1.

$$\sigma = K\left(\varepsilon_p + \left(\frac{\sigma_y}{K}\right)^{\frac{1}{n}} - \varepsilon_{plateau}\right)^n \quad \text{for } \varepsilon_p > \varepsilon_{plateau} \tag{5.1}$$

A BWH fracture model is used as a fracture criterion. The user-defined material model for this criterion in Abaqus(VUMAT) is developed by Mihkel Korgesaar, Professor at TalTech University. A comparison between no fracture and the BWH-criteria is shown in Figure 5.14.

The resulting stress-strain curve used in the crushing analysis is shown in Figure 5.9. Here it can be seen that the mean value of the S235 steel has a close correspondence to the S315 steel.

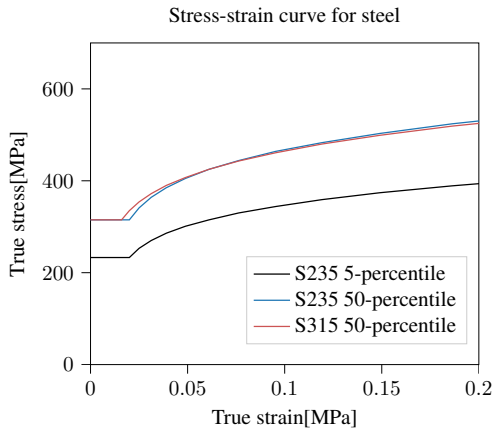

Figure 5.9: Stress-strain curve

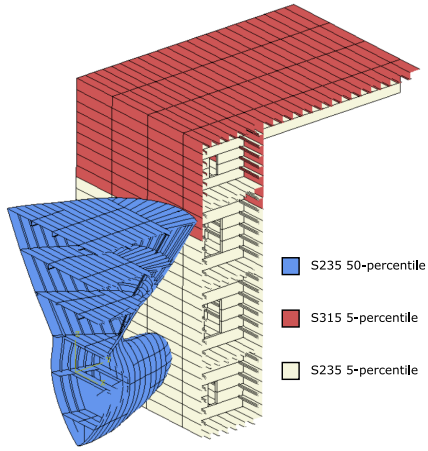

Figure 5.10: Material types

5.4 Model verification

An introductory crushing analysis was performed to verify the bow-model, the boundary conditions, and the materials. The analysis is similar to a head-on decoupled analysis, but the FPSO is made of rigid elements. This means that all energy is dissipated in the bow, which can be seen in Figure 5.11. The FPSO is fixed in all DOFs at the reference

point of the FPSO, while all other nodes are free since the element is rigid. The reference point is situated in the right corner of the figure. However, this position is not important as all DOFs are fixed,

The OSV-bow is defined to have an initial speed of $1m/s$. The velocity is chosen for convenience as the displacement will be equal to time. It is also important not to have a velocity that is too high, as this can cause instabilities in the analysis. A too low velocity, on the other hand, will make the analysis less time-efficient. A constant velocity of $1m/s$ is applied to the ship COG, which is connected to the bow with a kinematic coupling constraint.

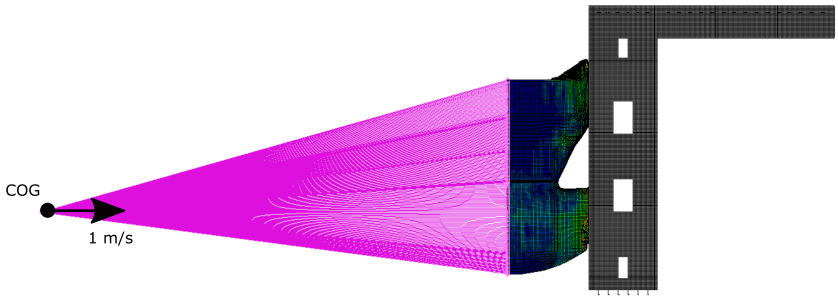

Figure 5.11: Analysis set-up for verification analysis. Bow is deformable, and FPSO-side is rigid.

The load-deformation curve for the bow can then be achieved. Storheim (2016) results are used for comparison and validation. The load-deformation curve obtained is shown in Figure 5.12, which is the total forecastle and bulb loads. The orange curve shows the results from Figure 6.3 in Storheim (2016), and the blue curve shows the results from the introductory analysis. A green curve illustrating a general force-deformation relationship from DNVGL-RP-C204 (2017) is also included. It can be seen that the results from this analysis have a slightly higher reaction force than what Storheim presents, but show a good correspondence to the DNVGL curve. The general pattern of load peaks corresponds well to Storheim, for example, the big increase when the bulb makes contact at 1.2 meters and the second deck at 2.2 meters.

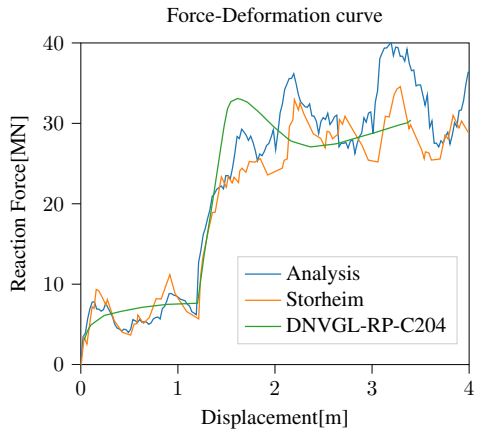

Figure 5.12: Force-deformation curve comparison with Storheim (2016).

There are several reasons for the deviation to the Storheim curve. The main reason is that the results from Abaqus consequently show higher reaction forces than the FE-software LS-DYNA, which Storheim used. This can be seen in the comparison between Abaqus and LS-DYNA in the Appendix in Figure B.1a retrieved from Storheim (2016). Another reason for the deviation, although found to have a minor effect, is that the S235 steel stress-strain curves are different. DNVGL-RP-C208 (2016) updated the recommended stress-strain curve, which is being used for this thesis. The stress-strain curves are shown in Figure 5.13.

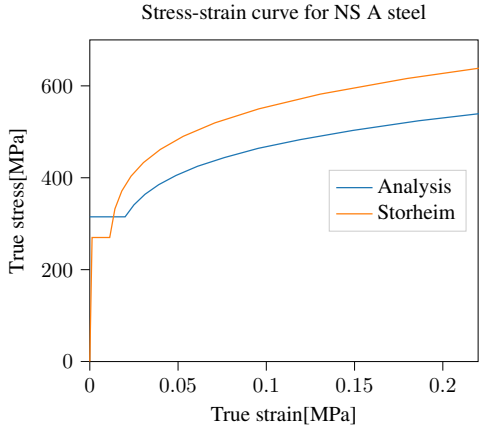

Figure 5.13: Stress-strain curve comparison

It should also be noted that the BWH fracture criteria are used for this thesis, while Storheim has utilized the RTCL criteria. These criteria show very similar behavior and are not likely to have a significant impact on the deviation. A comparison of these criteria can be seen in Appendix B.2, which is retrieved from Storheim (2016). A comparison of the BWH-criteria and no fracture can be seen in Figure 5.14. As expected, the curve for no fracture results in the highest reaction forces. This curve does not have significant local minima and maxima as the curve representing fracture, which is reasonable.

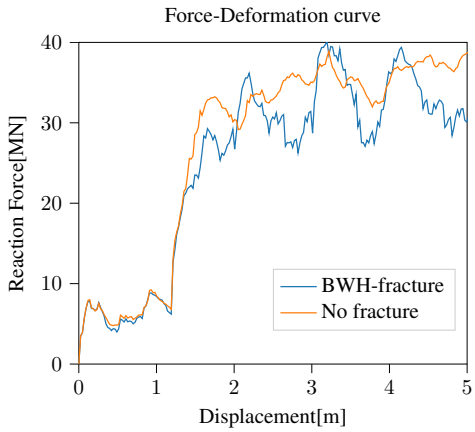

Figure 5.14: Effect of fracture criteria

The energy dissipation in the collision can be seen in Figure 5.15. The internal energy is the energy dissipated by the bow, and the artificial strain energy is the hourglass energy that occurs because of the utilization of reduced integration elements. An increase in energy dissipation can be seen when the bulb makes contact at 1.2 meters. This is reasonable as it is stronger than the forecastle, and therefore will dissipate more energy. After the first 0.1 seconds of the impact, the ratio of hourglass energy to internal energy stabilizes at 5%. This is at the upper limit of what is recommended in DNVGL-RP-C208 (2016). To improve this, either a refined mesh or full-integration elements can be used. Because both these actions have significant trade-off regarding computer efficiency, it was decided that the hourglass energy level was acceptable.

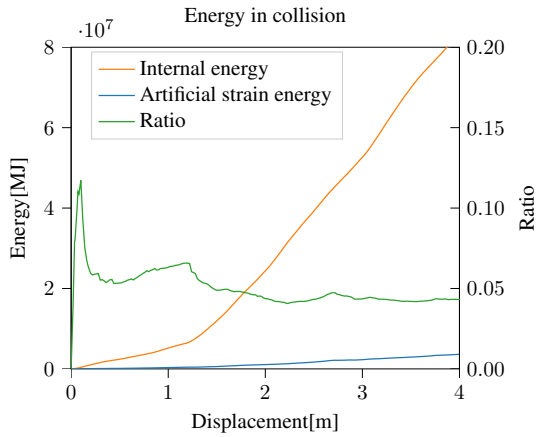

Figure 5.15: Influence of artificial energy on internal energy.

5.4.1 Verification of ice-reinforced bow

The same analysis set-up is used for the ICE-1C class bow. Figure 5.16 show the resulting load-deformation curve. Compared to the standard bow, it is about twice as strong, which is reasonable compared to the reference curve from DNVGL-RP-C204 (2017). It is also observed that the bulb makes an impact after 0.8 meters in opposite to 1.2 meters for the standard bow. This is an important observation because the high-strength bow will make contact with the struck structure at an earlier stage of the collision.

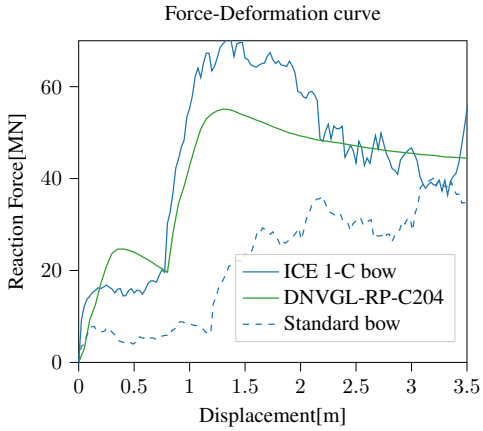

Figure 5.16: Load-deformation curve for ICE-1C class OSV-bow. The standard bow and the curve from DNVGL-RP-C204 (2017) is included for reference.

5.5 Analysis scenarios

The different collision scenarios in this thesis are presented in the next pages. The ICE-1C class OSV-bow is analyzed for the same coupled scenarios as the standard bow. The scenario name is differentiated by changing 'SC' to 'ICE' while the number represents the same analysis set-up.

A summary of all scenarios can be found in Table 5.8. The collision's most critical consequence is damage to the FPSO, and collision scenarios are therefore chosen with this in mind. This means a first impact position in the middle between two transverse web frames. It is also possible to select the conditions, so the horizontal stringer plates in the FPSO has a small strength contribution as possible. However, this is not opted for because realistic vessel drafts were prioritized.

The first distinction between the scenarios is the draft of the colliding vessels. Two different configurations are assumed, one for a fully loaded FPSO, and one for FPSO in ballast condition. These can be seen in Figure 5.17a and Figure 5.17b respectively. The draft for the fully-loaded and ballast condition FPSO is $24m$ and $16m$, respectively. The ballast draft is an assumption based on the loading capacity of FPSOs with similar main dimensions. This is because the general FPSO drawings used for the model in this analysis do not show the ballast draft. As shown in Table 5.6 a storage capacity of 1 million barrels(bbl) is reasonable. By assuming a crude oil-density of $900kg/m^3$, this equals a storage load of $130000tons$. This makes a ballast draft in between 16 and 17 meters reasonable, where the first is chosen to minimize boundary condition errors at the bottom of the FPSO.

Table 5.6: Comparable FPSO dimensions and storage capacity. Data is retrieved from FPSO.com (2020) and MarineTraffic (2020).

FPSO	L[m]	B[m]	Storage[Th. Bbl]
Johan Castberg	295	55	1100
Åsgård A	278	45	920
Skarv	292	51	880
Jotun A	232	42	584
Analysis model	295	58	1000

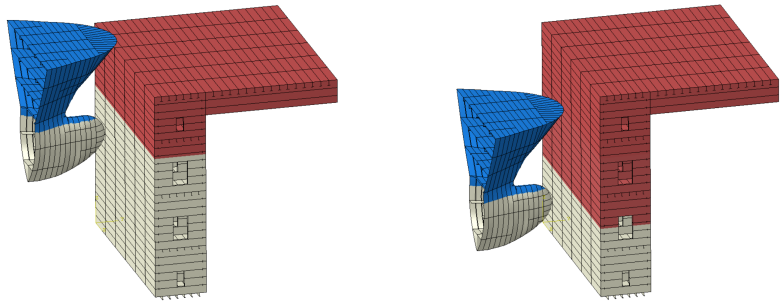

(a) Head-on collision and maximum FPSO-draft.

(b) Head-on collision and FPSO in ballast condition.

Figure 5.17: Collision scenarios for head-on collision. White color shows surface below waterline.

Oblique impacts are studied for impact angles $45°$, $60°$ and $75°$, where $90°$ is defined as head-on collision. Both drafts discussed above is analyzed. An example of the collision setup for impact angle $45°$ is shown in Figure 5.18.

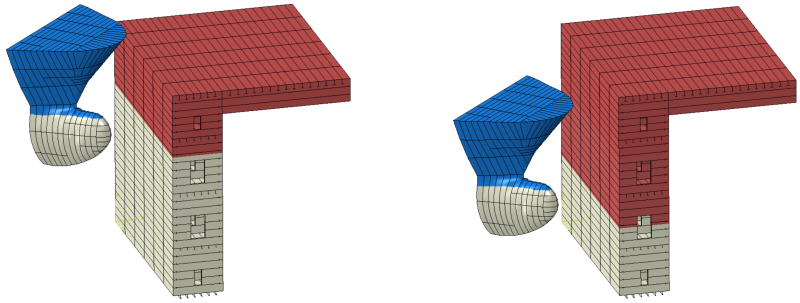

(a) Oblique collision of $45°$ and maximum FPSO-draft.

(b) Oblique collision of $45°$ and FPSO in ballast condition.

Figure 5.18: Collision scenarios for oblique impact. White color shows surface below waterline.

For the ICE-bow, a modification is done for the full load condition. The ice-strengthened OSV-bow has the second deck about half a meter above the FPSO main deck for full load condition. For ship collisions, both energy dissipation and physical penetration are of interest. The second deck will have a substantial impact on both factors, which is

important to consider. It is therefore decided to run two different analyses for all full load conditions with the ice-strengthened bow. For the modified scenario, the FPSO is moved 0.8 meters upwards to include the effect of the second deck. The configuration with equivalent drafts as the standard OSV-bow is shown in Figure 5.19a, and the modification is shown in Figure 5.19b. For reference, the same view for the standard bow is included in Figure 5.19c. It can be seen that the modified scenario has more similarities to the standard bow, as both will have a second deck with a strong impact. The resulting differences will be discussed in Section 6.4. It was not decided to do the same modification for the standard bow. The reason for this is that this would mean that the OSV has a lower displacement. The collision energy would, therefore, be lower for the same velocity. An increased velocity is an option, but it was decided to focus on the fully-loaded OSV.

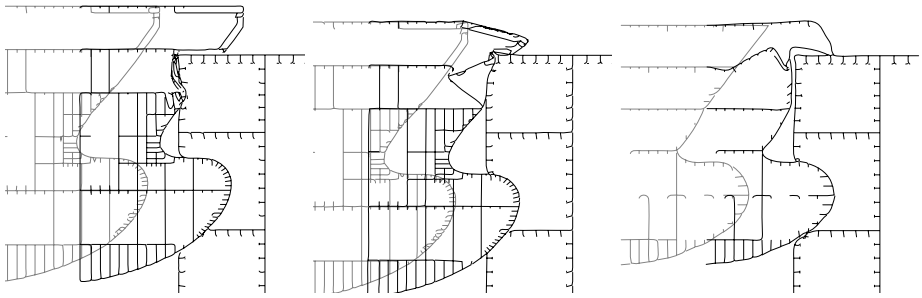

(a) (b) (c)

Figure 5.19: Effect of second deck for full load condition.

The boundary conditions for both the coupled model and the decoupled model discussed in Section 5.1.1 are applied for the respective scenarios. Moan et al. (2019) suggests that the minimum impact energy in bow impact should be 50*MJ*. This impact energy is therefore used for calculating the impact speed for all the coupled simulations. The x- and y-components of the velocity for the different impact angles are shown in Table 5.7. The calculation is done by manipulating the equation for kinetic energy, which can be seen in Equation 5.2.

$$E_k = \frac{1}{2}(M + A)V^2 \tag{5.2}$$

$$V^2 = \frac{2E_k}{M + A} \tag{5.3}$$

where A is the added mass equal to 0.1M, E_k is the kinetic energy and

$$V^2 = (V \cdot cos(\alpha))^2 + (V \cdot sin(\alpha))^2 = V_x^2 + V_y^2.$$

Table 5.7: Velocity components corresponding to E_k=50MJ

	90°	75°	60°	45°
V_x [m/s]	0	0.9	1.75	2.47
V_y [m/s]	3.50	3.38	3.03	2.47

Table 5.8: Collision scenario summary

Scenario	FPSO draft	Angle	Coupled
SC 1	Full	90	No
SC 2	Full	75	No
SC 3	Full	60	No
SC 4	Full	45	No
SC 5	Full	90	Yes
SC 6	Full	75	Yes
SC 7	Full	60	Yes
SC 8	Full	45	Yes
SC 9	Ballast	90	No
SC 10	Ballast	75	No
SC 11	Ballast	60	No
SC 12	Ballast	45	No
SC 13	Ballast	90	Yes
SC 14	Ballast	75	Yes
SC 15	Ballast	60	Yes
SC 16	Ballast	45	Yes

6 Analysis of ship collision

The analysis results for the scenarios discussed in Section 5.5 will be presented in this chapter. Relevant comparisons will be presented, for example, deviations between the coupled and decoupled method, impact angle, and FPSO loading condition. All coupled analyses have an initial collision energy of 50MJ. However, not all of the energy will be dissipated as strain energy in two colliding structures. Depending on the scenario, a significant amount of energy is dissipated as friction. For some scenarios there are also remaining kinetic energy after the collision. This energy is not included in the load-deformation curves presented in this section, which explains why the area below the curves is less than the initial impact energy of 50MJ. The scenario names presented in the previous section will be written in *italic*. For the figures showing contour plots of the structure deformation, the legend is not included because of readability. The scale for these figures is Von-Mises stress from zero to max stress, blue to red color. For most of this chapter, results are presented for the full load condition and ballast condition in separate plots. This was chosen to not include too much information in one plot.

6.1 Coupled analysis

The results from the coupled analyses will be presented in this section. Several results are reasonable to present together, which means that there are some occasions where the mentioned figure is situated on the next page. The dissipated energy distribution for each collision scenario is shown in Table 6.1. E_{total} is the sum of the energy dissipated by the FPSO and OSV, E_{fpso}, and E_{osv}, respectively.

Table 6.1: Energy dissipation in coupled analysis

	SC5	SC6	SC7	SC8	SC13	SC14	SC15	SC16
E_{fpso} [MJ]	15.5	21.2	7.8	2.9	18.9	16.8	10.6	0.4
E_{osv} [MJ]	27.7	20.5	22.7	10.1	26.4	28.5	23.8	7.9
E_{total} [MJ]	43.2	41.7	30.5	13.0	45.2	45.3	34.5	8.4
E_{fpso}/E_{osv}	0.56	1.03	0.34	0.29	0.72	0.59	0.45	0.05
$E/E_{kinetic}$	0.88	0.83	0.76	0.55	0.90	0.91	0.69	0.17

In Table 6.1, it can be seen that the OSV dissipates more energy than the FPSO for all scenarios but one. Nevertheless, for most of the scenarios, the FPSO dissipates more than 25% of the total energy. This makes the shared-design principle discussed in Chap-

ter 3 the correct assumption. Furthermore, it can be seen that the total energy dissipated decreases for sharper collision angles.

The kinetic energy during the impact for all coupled analyses can be seen in Figure 6.1. The added mass coefficient is constant for all analyses, which means that the kinetic energy suits as a visualization of the velocity magnitude during the impact. The only collision scenario that has significant velocity after impact is *SC16*. In this case, the kinetic energy has decreased by approximately 30%. For collision scenario *SC8* and *SC15*, it can be seen that the velocity decrease slower than for less sharp angles, which means more sliding motion has occurred.

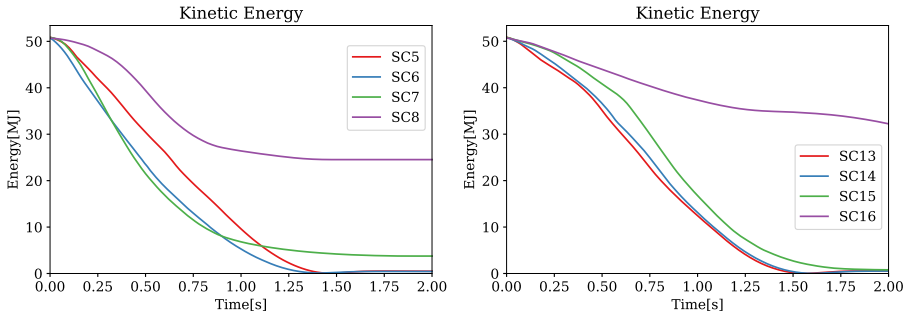

(a) Full load condition

(b) Ballast condition

Figure 6.1: Kinetic energy during impact for all coupled scenarios.

The corresponding friction dissipation curves are shown in Figure 6.2. It is observed that sharper angle impacts have higher dissipated friction energy. It is also noted that the head-on scenarios *SC5* and *SC13* dissipates friction energy. The reason is that there are substantial friction forces between the structures during a collision, even if a global sliding motion does not occur. However, for both loading conditions, the head-on impact dissipates the lowest friction as expected.

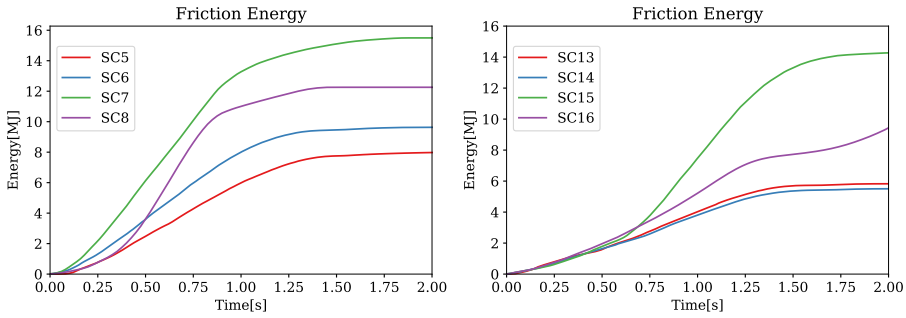

(a) Full load condition

(b) Ballast condition

Figure 6.2: Friction energy dissipation during impact for all coupled scenarios.

The load-deformation curves for the fully loaded- and ballast-condition coupled analyses are shown in Figures 6.3 and 6.4 respectively. The axis on the figures are equal, and a distinct difference between the two loading conditions can be observed. In general, it can be seen that the reaction forces are higher from the initial point of impact for the fully loaded FPSO condition. The main reason for this is the earlier impact of the bulb. However, the early impact of the bulb does not necessarily mean more serious damage on the FPSO. As in scenarios *SC7*, *SC8* and *SC15* where there can be seen an early peak resistance for the FPSO. The reason for this is that the oblique angle of $45°$ and $60°$ make the bulb make an impact with a web frame in the FPSO, which is a lot stronger than the plating between. In Figure 6.6, visualizations of the bulb impact on the FPSO side can be observed. It can also be seen in Figure 6.2 that a substantial amount of friction energy is dissipated for *SC7*, *SC8* and *SC15*. This is caused by the oblique angle, which causes tangential friction forces from a sliding motion.

For scenarios *SC5*, *SC6*, *SC13* and *SC14* it can be seen that the energy dissipation are similar. For these scenarios, a sticking collision behavior is dominant, which means neglectable sliding motion. This can be observed in the Figures 6.1 and 6.2 which is showing kinetic and frictional dissipation dependent on time. All scenarios have a relatively low percentile of friction dissipation compared to the total energy dissipation. The kinetic energy is also falling faster than for sharper impact angles, which indicates that there is less sliding motion. It should be noted that there will always be an amount of friction for sticking collisions modes as well since the high impact force and material contact induce high friction forces.

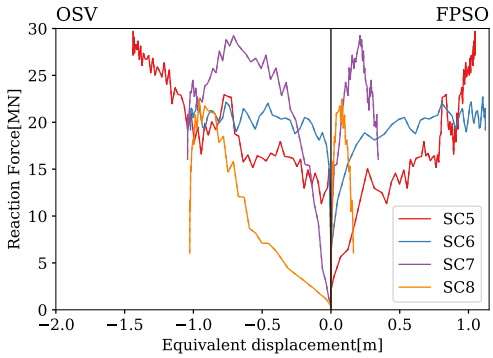

Figure 6.3: Oblique impacts for FPSO in fully loaded condition.

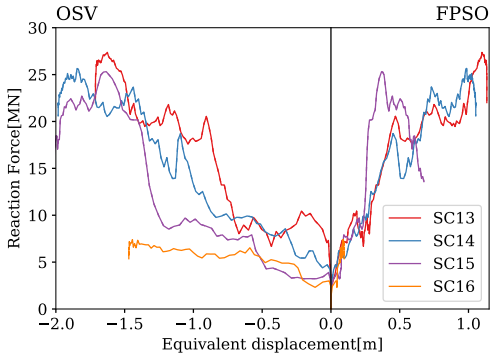

Figure 6.4: Oblique impacts for FPSO in ballast condition.

As seen in Table 6.1, the two $45°$ impact angle scenarios result in very little damage to the FPSO. The OSV damage is also limited, compared to the scenarios with less sharp angles. Only about 26%(*SC8*) and 17%(*SC16*) of the initial kinetic energy is dissipated as internal energy in the two structures. Approximately the same amount is dissipated as friction energy, while the rest of the energy remains as kinetic energy as the OSV will drift off. This can be seen in Figures 6.2 and 6.1. Here it is also evident that *SC7* also has a remaining velocity after impact. However, the magnitude of this velocity is very close to zero.

The equivalent displacement at the x-axis of the load-deformation curves illustrates the amount of deformation of the structures. However, this is not necessarily the exact

deformation, but it serves as a good option for deformation comparison. It is observed that the displacement of the OSV bow for ballast condition is up to twice as large as the fully loaded condition. The area below the curves, i.e., the dissipated energy, is, on the other hand, very similar. The reason for this is that the first-mentioned condition results in a lot more deformation of the forecastle, which is relatively weak compared to the bow and the FPSO side. This strength difference has a bigger impact on the resulting energy dissipation for lower energy collisions. For example, an impact energy of 10MJ, which is equivalent to an initial velocity of 1.6m/s. In Figure 6.5 a collision energy of 10MJ is marked on for the head-on scenarios shown on the Figures 6.3 and 6.4, but the axes are different for better visibility. Here it is seen that the FPSO dissipates the majority of the energy for *SC5* and the opposite for *SC13*. The reason for this is that the stronger bulb cause neglectable damage for *SC13*, while it causes the majority of the damage for *SC5*. It is worth noting that this result is obtained from the load-deformation curve of a collision energy of 50MJ. This is not assumed to make a significant impact on the result, which will be further discussed in Section 6.3

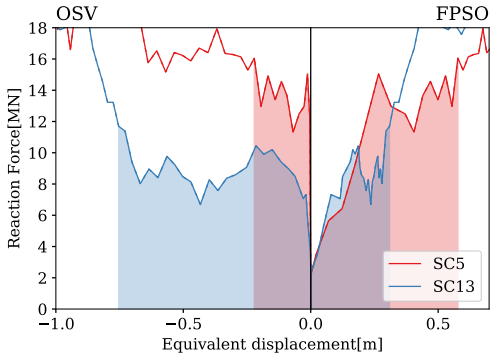

Figure 6.5: Head-on impact for a 10MJ collision energy

FPSO material and geometry are also affecting the results. The FPSO is strengthened with a high tensile steel and higher plate thickness at the top part, which can be seen in Figure 5.6b and 5.10. When the FPSO is fully loaded, the OSV-bulb will impact partially on this strengthened structure. For ballast condition, the bulb is not in contact with the high tensile steel. Since the bulb is causing most of the damage on the FPSO, this has a strong effect on the final result. It could have been expected that the fully loaded condition had the most damages on the FPSO as the bulb makes an earlier impact, but it is seen that this is not always the case.

In Figure 6.6, the structural damage from the bulb on the FPSO is shown for $90°$ and $60°$ impacts. The figures are viewed from the back of the FPSO to show the inner FPSO-

structure. The pictures are captured at the end of each collision, which makes it possible to see traces from potential sliding, for example, for *SC7* where the sliding motion is evident. A horizontal stringer plate can be seen in all figures. This feature has a strong impact on the FPSO-side collision resistance. The origin of the high peak resistance for *SC15* can be observed in Figure 6.6d. Here it is seen that the first impact of the bulb is at the transverse web frame, while the stringer plate also has a strength contribution. The crosses between transverse web frames and horizontal stringers are the strongest parts of the FPSO-side model, explaining the high resistance for *SC15*. The low resistance of *SC5* is also evident in Figure 6.6a as there is a minimal contribution from the transverse web and stringer. The corresponding deformation from the forecastle is not of the same magnitudes and can be found in the Appendix in Figure D.1.

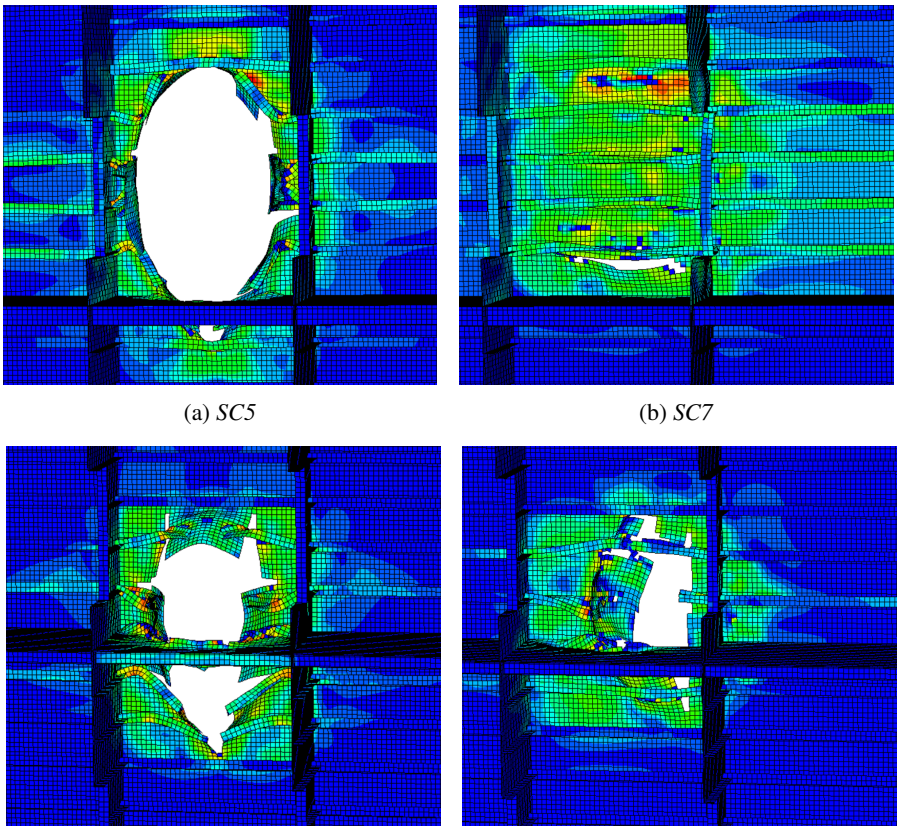

(a) *SC5* (b) *SC7*

(c) *SC13* (d) *SC15*

Figure 6.6: Structural damage from bulb on the FPSO-side for selected scenarios. The view is from the back of the FPSO-side viewing towards the OSV.

In the paragraphs above, the focus has been on energy dissipation. However, it is not clear from the load-deformation curve for what scenario the physical penetration in the normal plate direction of the FPSO-side is the largest. This is an important result as the largest consequence of a collision with an FPSO is penetration to the petroleum storage tanks.

The three scenarios where the FPSO has the most penetration are presented in Figure 6.7. It can be seen that the most critical scenario is *SC5*, where the bulb penetrates the FPSO side about halfway in. The scenario with most energy dissipation by the FPSO is *SC6*, but this has an impact angle of 75°, which makes more of the energy dissipation occur in the transverse direction. It is, therefore, safe to say that there will not be any penetration of the inner FPSO plating for a collision energy of 50MJ.

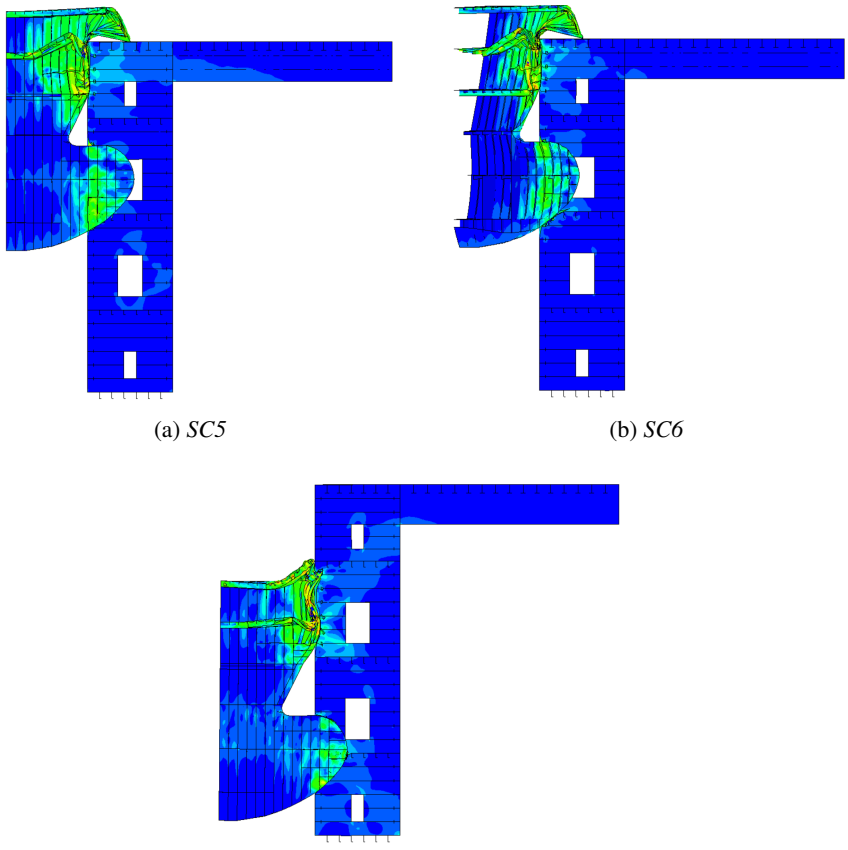

(a) *SC5*

(b) *SC6*

(c) *SC13*

Figure 6.7: Maximum penetration for the three most critical scenarios.

6.2 Comparison with analytical external dynamics formulation

The energy calculated by the external mechanics method discussed in Section 3.2 is presented in Table 6.2 as E_a. The script is only verified with the results Liu and Amdahl (2019) for the sticking case. With an effective friction factor of $\mu_0 = 0.6$, the sticking condition was fulfilled for all scenarios, except the $45°$ impacts. For the $45°$ scenarios, *SC8* and *SC16*, the sliding condition is used and is marked with an asterisk in the table. This part of the routine is more complicated to implement and was not finalized in due time for this thesis. The results from the verification with Liu and Amdahl (2019) are presented in Appendix E together with the code used.

It is seen that the deviation for the sticking scenarios is relatively small, with a deviation below 10%. The sliding impacts marked with an asterisk are included for reference but are not verified. These results show that the simplified method can be an effective method to give a reasonable estimation of the external dynamics for a ship collision without utilizing advance FE-software.

There are uncertainties regarding impact position and impact plane angle, especially for the full load FPSO condition. For both analyses, the impact plane is assumed to be a vertical plane along the FPSO-side. However, the forecastle makes for the full load condition case contact at the top corner of the FPSO, which makes it challenging to choose a local plane angle.

Table 6.2: Multiplanar impact comparison

	SC5	SC6	SC7	SC8	SC13	SC14	SC15	SC16
E [MJ]	43.2	41.7	30.5	13.0	45.2	45.3	34.5	8.4
E_a [MJ]	48.9	41.3	33.7	24.7	48.8	41.3	33.7	24.7
Diff. [MJ]	-5.7	0.4	-3.2	-11.7*	-3.6	4.0	0.8	-16.3*

6.3 Comparison with decoupled analysis

A comparison of the load-deformation curves for the coupled and decoupled analysis is shown in Figure 6.8 and 6.9. The coupled analysis are shown as dotted lines, and the decoupled analysis are shown as solid lines. It can be seen that there is good correspondence at the majority of the collision period for the full load condition. The results are deviating more for the ballast condition, but there is a relatively good correspondence here as well. There are more deviations at the end of the coupled impact period, which is reasonable as this is where the coupled effects have developed the most. It is also noted that there is no significant deviation for the decoupled method energy dissipation accuracy, depending on the impact angle.

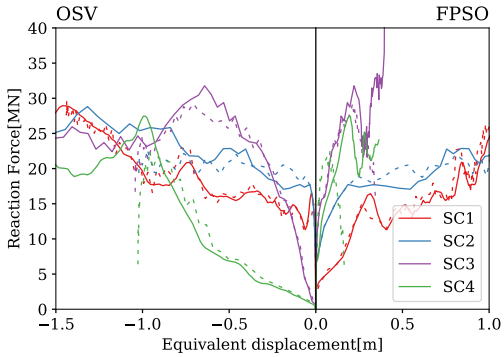

Figure 6.8: Coupled analysis are shown in dotted lines and decoupled analysis as solid lines.

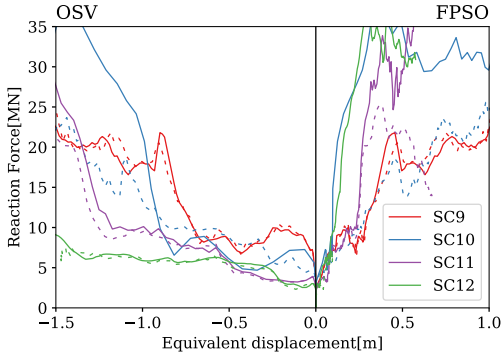

Figure 6.9: Coupled analysis are shown in dotted lines and decoupled analysis as solid lines.

6.3.1 Penetration paths

The penetration path for selected scenarios is shown in Figures 6.10 and 6.11. This path is from the motion of a point in the back of the bow at the same height as the COG. This point is not affected by the impact because of its position in the back but captures the motion of the bow well. The penetration path does not describe how the structural deformation or energy dissipation will be distributed. The red curve shows the decoupled path, which has a constant direction for the whole impact period. The green curve shows the path for coupled analysis when the FPSO is in a fully loaded condition, and the red curve shows the coupled analysis for ballast condition. As expected, it can be seen that the deviation increases for sharper collision angles.

The distance from the red dot marking the initial impact and the end of the coupled analysis curves illustrates for what scenarios the backside of the bow has moved the furthest after impact. This can indicate the scenario with maximum penetration of the FPSO-side, but this is also depending on the strength of the bow as discussed above. In addition, when the bulb first makes an impact, it will also strongly affect the actual penetration of the FPSO. These curves can also indicate the amount of energy dissipation in the collision. As anticipated, it is observed that more internal energy is dissipated when the penetration distance in the y-direction is larger. However, as discussed in Section 6.1 this is only an indication as deviations may occur depending on materials, geometries, and impact angle.

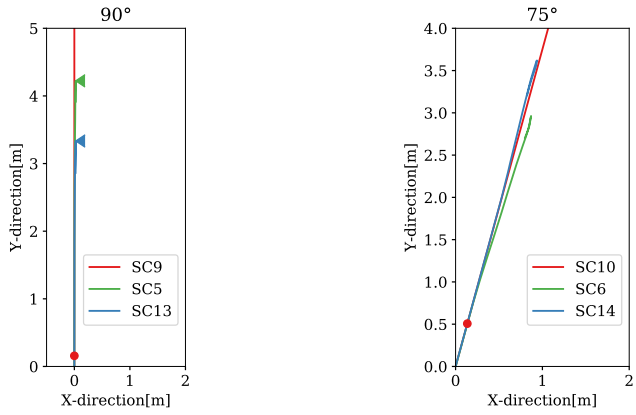

(a) (b)

Figure 6.10: Penetration paths for impact angles $90°$ and $75°$. Red point marks first point of impact. The green and blue triangles in Figure 6.10a is the maximum displacement for *SC5* and *SC13*.

For impact angles $75°$ and $90°$ shown in Figure 6.10, it can be seen that the penetration path for the coupled analysis follows the decoupled analysis well. It is also shown that the max displacement when the FPSO is in a fully loaded condition, *SC5*, is higher than for the ballast condition, *SC13*. The reason for this is the earlier impact of the strong bulb, which increases the relative strength of the bow for the first part of the collision compared to *SC15*.

The penetration path can show the amount of sliding and sticking during the collision. For collision angle $45°$, a sliding motion occur for both *SC15* and *SC16* shown in Figure 6.11b. This can be seen by observing that there is little movement in the y-direction, but more and more in the x-direction. There are also sliding motions for $60°$ as shown in Figure 6.11a, but for *SC7* it is seen that the OSV come to a full stop, i.e no drift off. This result can also be seen in the plot for kinetic energy shown in Figure 6.1. The reason for the drift-of motion originates from the eccentricity in the x-direction between the bow and the COG of the OSV for oblique impacts. This leads to a rotating moment that induces the ship's yaw-motion. This effect makes the bow leave the FPSO at the time the y-velocity equals zero, which can be seen in, for example, *SC5* and *SC7* Since there are no wave radiation effects included in the coupled model there are no forces that decelerate this rotation.

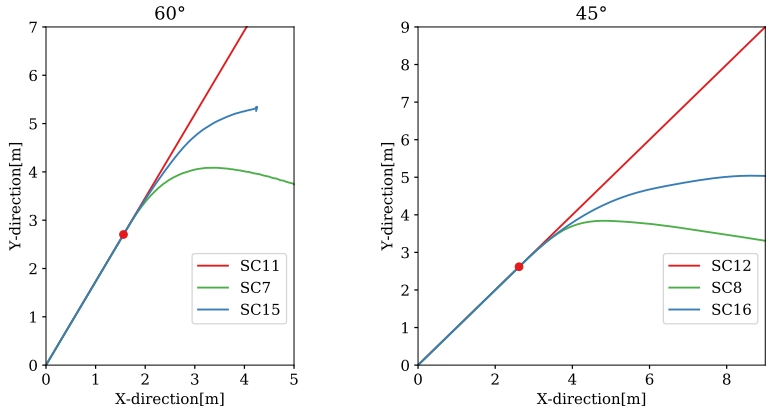

(a) (b)

Figure 6.11: Penetration paths for impact angles $60°$ and $45°$. Red point marks first point of impact.

The results presented in this section show that the decoupled method's energy dissipation gives relatively good predictions for all impact angles compared to the coupled model. This can be seen in Table 6.3, where the energy dissipation distribution between

the OSV and FPSO is compared. It is shown that the difference in energy dissipation for each stricture is below 2MJ for all but *SC11*. This accurate prediction of energy dissipation has also been obtained by Tabri (2012), who performed experimental, coupled and decoupled collision analyses. Here it was also found that the penetration paths were deviating more, especially for sharper collision angles. More specific, the decoupled analyses overestimate the normal penetration of the ship-side, while underestimating the transverse penetration. This result is also observed for the analyses in this thesis seen in Figure 6.11. In general, it can be said that decoupled analyses have good accuracy for head-on collisions close to the struck ship COG, both for energy dissipation and penetration path. When the impact point and angle changes, the ship motions become more complex, and the decoupled method's validity becomes questionable.

Table 6.3: Energy dissipation for coupled and decoupled analysis

	SC1	SC2	SC3	SC4	SC9	SC10	SC11	SC12
E_{osv} [MJ]	27.2	20.4	23.9	9.2	24.4	29.2	28.4	7.9
$E_{o,coup}$ [MJ]	27.7	20.5	22.7	10.1	26.4	28.5	23.8	7.9
Diff. [MJ]	-0.5	-0.1	1.2	-0.9	-2.0	0.7	4.6	0.0
E_{fpso} [MJ]	16.0	21.3	6.6	3.8	20.9	16.1	6.0	0.4
$E_{f,coup}$ [MJ]	15.5	21.2	7.8	2.9	18.9	16.8	10.6	0.4
Diff. [MJ]	0.5	0.1	-1.2	0.9	2.0	-0.7	-4.6	0.0

Tabri (2012) assumed a homogeneous ship-side structure for the analyses. As discussed in Section 6.1, the geometry, material, and impact position will have an evident effect on the difference between the coupled and decoupled analyses. The ship motion after the first impact will change depending on the resistance in the FPSO-side. The results in this thesis are therefore influenced by the strength differences in the ship side, which can make the results deviate from Tabri (2012) for some scenarios.

In Figures 6.12 and 6.13, penetration paths for scenarios where the FPSO position is moved 2 meters along the x-axis is shown. The data from Figures 6.10 and 6.11 is also included for comparison purpose. It can be seen that the changed geometry at the impact point has a clear effect on all scenarios. For the impact angles of $75°$ and $90°$, it can be seen that the y-displacement decreases significantly. The reason for this is that the shifted FPSO means that the OSV-bow makes an impact right at a strong transverse web frame. Hence, the velocity of the ship decreases faster. There are also differences for $60°$ and $45°$, however, not that evident as the two less sharp-angled impacts.

These results make it reasonable to conclude that the scenarios discussed in Section 6.1 are suitable choices concerning the most critical scenario. The only outlier by inspecting the penetration paths is *SC7*. This is probable to cause more damage to the FPSO if it is

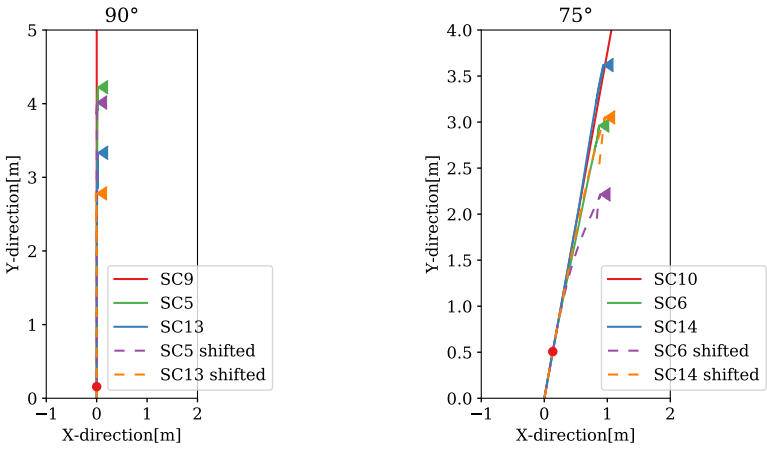

(a) (b)

Figure 6.12: Penetration paths for impact angles 90° and 75° including analyses with the FPSO shifted 2 meters. Red point marks first point of impact and triangles marks maximum displacement in the y-direction.

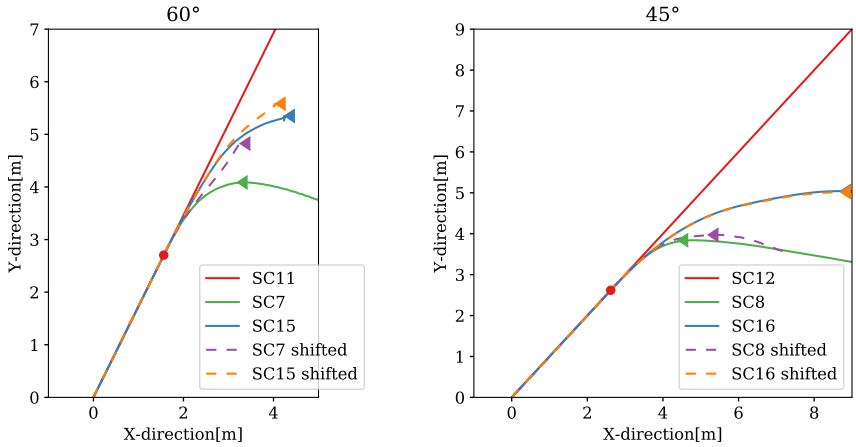

(a) (b)

Figure 6.13: Penetration paths for impact angles 60° and 45° including analyses with the FPSO shifted 2 meters. Red point marks first point of impact and triangles marks maximum displacement in the y-direction.

shifted 2 meters. This can also be seen in Figure 6.3, where *SC7* shows a stronger FPSO than the other scenarios. However, the total dissipated energy of 30.5MJ is not likely to change a lot. This means that this scenario can cause more damage to the FPSO than presented, but not as much as the most critical scenarios.

6.4 Ice-reinforced bow

The increased strength from an ice-strengthened bow leads to a different collision result and is described in this section. The modified condition for full load condition, where the FPSO has 0.8 meters less draft than the maximum as described in Section 5.5, is discussed first because this is comparable to the standard bow configuration. The original condition is presented afterward. The kinetic and friction energy dissipation is very similar to the standard bow results and can be found in the Appendix in Figures C.2 and C.3 for reference.

Table 6.4 show the energy dissipation for the FPSO and the OSV as well as the difference to the standard bow denoted as *Diff.* in the table. For most scenarios, the FPSO is dissipating less energy than when it is struck by the standard bow. This result may be surprising since the ice-strengthened bow is about twice as strong as the standard bow, as seen in Figure 5.16.

Table 6.4: Energy dissipation for ice-reinforced bow

	ICE5	ICE6	ICE7	ICE8	ICE13	ICE14	ICE15	ICE16
E_{fpso} [MJ]	17.4	14.4	14.4	0.8	16.0	12.7	7.2	1.1
Diff.	+1.9	-6.8	+6.6	-2.1	-2.9	-4.1	-3.4	+0.7
E_{osv} [MJ]	27.5	29.7	19.4	9.2	29.8	30.7	20.1	7.8
Diff.	-0.2	+9.2	-3.3	-0.9	+3.4	+2.2	-3.7	-0.1
E_{total} [MJ]	44.9	44.1	33.8	10.0	45.8	43.4	27.2	9.0
Diff.	+1.7	+2.4	+3.3	-3.0	+0.6	-1.9	-7.3	+0.6

The reason for this can be explained by inspecting scenario *SC13*. Figure 6.14 shows the energy dissipation distribution for this scenario. It is observed that that the velocity, visualized by the kinetic energy, decreases faster for the ice-bow collision. The main reason for this result is that the forecastle of the ice-strengthened bow is much stronger than the standard bow, which can be seen in Figure 5.16. The other reason for this is the influence of the strong web frames of the FPSO.

After about $0.1s$ of the collision, the FPSO dissipation curve for the ice-strengthened bow has a plateau, and at the same time, the bow starts to dissipate the energy. This point is where two web frames of the FPSO-side make contact with the OSV. These frames

increase the strength a lot, which means the bow will deform. Since the forecastle is much stronger for the ice-reinforced vessel, a lot more energy is dissipated. Hence, the velocity and, therefore, also the collision energy decreases faster. When the strong bulb makes contact after 0.3s, the remaining impact energy is more than 10MJ lower than for the standard bulb. In the end, this leads to less damage done by the bulb, which remains virtually undamaged for both cases.

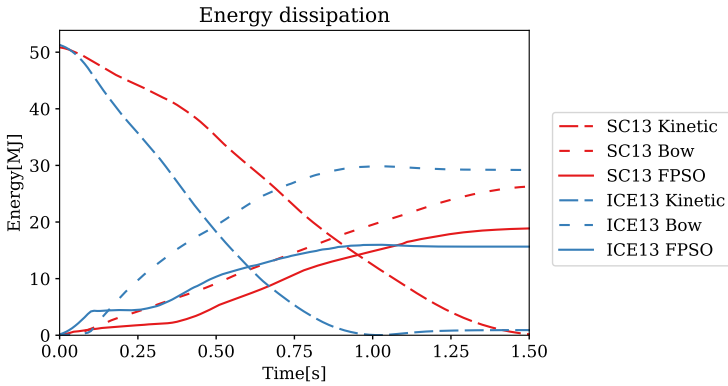

Figure 6.14: Energy dissipation ice-reinforced bow.

The load deformation-curves for the ice-reinforced bow is shown in Figure 6.15 and 6.16. The corresponding curves for the standard bow are shown as dashed lines in the same scenario color. It can be seen that the reaction force is higher for most of the scenarios. Furthermore, it is observed that the equivalent displacement is higher for the standard bow. This originates in increased strength from the forecastle discussed above. In Figure 6.16, it can be seen that the bulb makes an impact at an earlier stage of the impact period, which makes the damage on the FPSO bigger. However, this effect is canceled by the effect of the strong forecastle and transverse web frames of the FPSO.

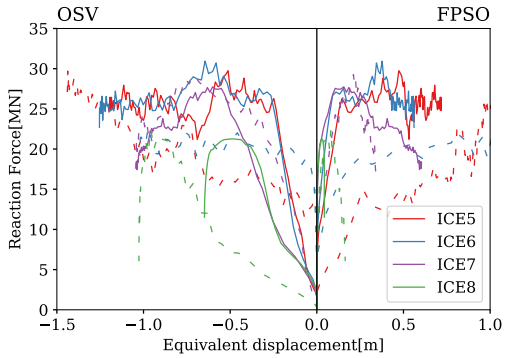

Figure 6.15: Load-deformation curve ice-reinforced bow for modified full load condition.

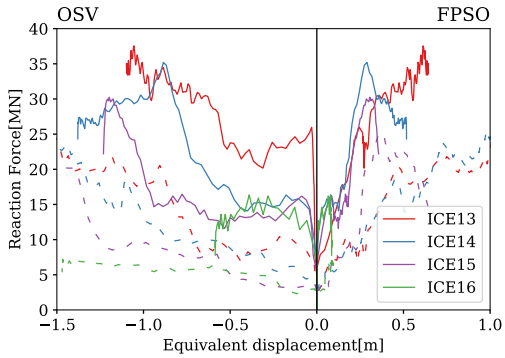

Figure 6.16: Load-deformation curve ice-reinforced bow for ballast condition.

For the original configuration for full load condition, the results are different. The strength contribution of the OSV second deck is for this configuration, not impacting the forecastle reaction force. As seen in Figure 6.17, the reaction force is at significantly lower level than for the modified scenario which is shown in Figure 6.15. It can further be observed that the FPSO is dissipating an increased amount of energy compared to the OSV: This can also be seen in Table 6.5. In this table, the difference from the modified condition is denoted as *Diff.*.

Table 6.5: Energy dissipation for ice-reinforced bow for original full loaded condition

	ICE5	ICE6	ICE7	ICE8
E_{fpso} [MJ]	20.1	19.6	20.8	27.6
Diff.	+2.7	+5.2	+6.4	+26.8
E_{osv} [MJ]	20.3	18.0	12.2	5.6
Diff.	-7.2	-11.7	-7.2	-3.6
E_{total} [MJ]	40.4	37.6	33.0	33.2

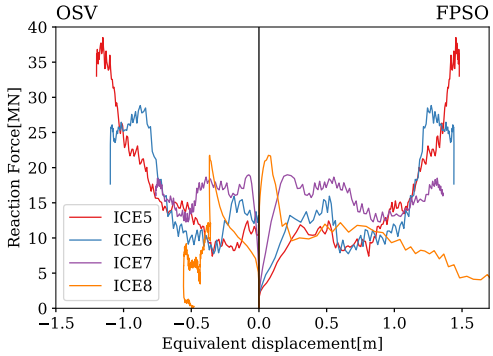

Figure 6.17: Load-deformation curve ice-reinforced bow for original full load condition.

A result that stands out is scenario *ICE8*, where the energy dissipation for the FPSO is the highest for all scenarios discussed in this thesis. By inspecting the load-deformation curve, a high peak at the beginning can be seen before it flattens out at about 10MN reaction force. This behavior occurs because the OSV forecastle impacts the FPSO first before pushing off without damaging the FPSO significantly. Then the bulb hits as a secondary impact, without any impact from the forecastle as this is rotating away from the FPSO. This prevents the sliding motion seen from the other $45°$ scenarios, and the bulb penetrates the FPSO-side with high kinetic energy left. It is important to note that the the x-axis in Figure 6.17 is cut at 1.6, however the curve for *ICE8* continues up to about 3.5 meters. This is not included in the figure due to the visibility of the other curves but is included in the Appendix in Figure C.1.

As discussed in Section 6.1, the maximum penetration is an important factor to consider, in addition to the energy dissipation. Three critical scenarios for the ice-reinforced bow is presented in Figure 6.18. Figure 6.7a is also included for reference, as this is the most critical scenario regarding penetration for the standard bow. It can be seen that *ICE5* is the scenario with the most penetration of the scenarios discussed in this thesis. For this

scenario, the bow has penetrated the FPSO-side 3.42 meters, which is about 61% of the side-width. However, there is not a big difference from the equivalent scenario for the standard bow. A table presenting the maximum penetration for all scenarios discussed in this thesis can be seen in the Appendix in Table C.1. Both scenarios have a penetration of slightly more than halfway through the FPSO-side. *ICE13* can be observed to have very little penetration, even though the FPSO energy dissipation for this scenario is not very different from *ICE5*. Scenario *ICE8* discussed above, does not cause a significant penetration in the normal direction to the FPSO-side, as the initial impact direction is 45°.

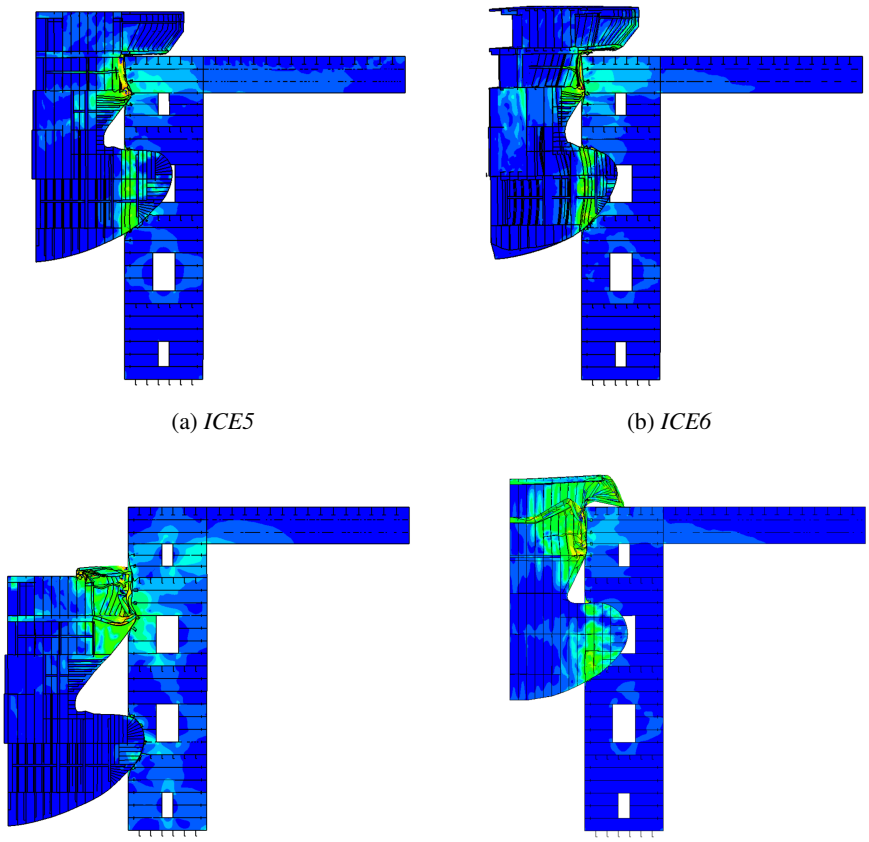

(a) *ICE5*

(b) *ICE6*

(c) *ICE13*

(d) *SC5*

Figure 6.18: Penetration of FPSO-side for ice-strengthened bow.

7 Conclusions and further work

The OSV impact does not cause rupture of the inner FPSO side-shell for any collision of 50MJ impact energy studied in this thesis. The maximum penetration of the side is found to be 61% of the FPSO side-width, which is for a head-on collision with an ice-reinforced bow. The most critical scenarios regarding penetration of the FPSO is, as expected, the $90°$ and $75°$ impacts. The geometry of the FPSO-side, especially the transverse web-frames, is found to have a significant impact on side penetration. While the forecastle makes contact with one or more transverse web frames for all analyses, there are scenarios where the bulb remain unaffected of this feature. The FPSO-geometry is also shown to have a significant effect on the penetration path for the coupled analyses.

The energy dissipation in the collision is found to be within the shared-energy design domain. In general, the OSV-bow dissipates more energy than the FPSO, which for most cases, dissipates between 20% and 40% of the dissipated energy in the collision. For the ice-reinforced OSV-bow, this trend is even more apparent. The reason for this is that the forecastle dissipates more energy than the FPSO side, because of the transverse web-frames. The maximum energy dissipation for the FPSO is found to be 27.6MJ for an ice-reinforced bow, and 21.2MJ for a standard bow. The OSV has a maximum energy dissipation of 30.7MJ and 28.5MJ for the ice-reinforced and standard bow.

There are no significant differences in energy dissipation distribution between the full load FPSO condition and the ballast condition for impact energy of 50MJ. However, for impact energies below 15MJ, the full load condition is found to be more critical to the FPSO. In this case, the FPSO is found to dissipate the majority of the impact energy.

The comparison between coupled and decoupled analyses shows that the decoupled analyses predict the energy dissipation to a satisfying degree. The penetration path, on the other hand, show more significant deviations. Especially for sharper impact angles, notable deviations are found. Both these findings correspond well to earlier work within this subject, for example in Tabri (2012).

The analytical method for calculating external dynamics presented in Liu and Amdahl (2019) shows a good correspondence to the results obtained in the coupled analysis. The prediction for the ”sticking” collisions, i.e., no sliding motion, is within 5MJ of the results obtained in the coupled analyses. This means that this method, together with the

decoupled analyses, can give relatively accurate results, especially for less sharp impact angles. It should be noted that there was no time to implement the sliding cases routine, which in this thesis is for impact angle $45°$.

There are no clear error sources assumed to make a significant impact on the final results. The effect of different boundary conditions has been verified, as well as the load-deformation curve for both ship models. The FPSO-side has not been compared to results from other similar structures. However, the structure has an expected deformation pattern and mesh continuity at all positions where continuity is sought after. Reduced integration is used for all analyses, which can be an error source, especially for coarse meshes. However, the hourglass energy is inspected and found to be lower than 5%, which is within DNVGL-RP-C204 (2017) recommendations. Possible mitigation's for the mentioned error sources is presented in Section 7.1

7.1 Further work

The coupled analyses in this thesis are based on a simplified method, where the hydrodynamic coefficients are assumed constant. A full coupled analysis, as proposed by Yu and Amdahl (2016), could be implemented in Abaqus. This method will result in more accurate results, especially for ship motions. As the decoupled method shows relatively good results for the energy dissipation, it is not expected that the full coupled method will have significant deviations from the simplified coupled method regarding energy dissipation. The analytical external mechanics model described by Liu and Amdahl (2019) can be used as a comparison and should be implemented for sliding impacts as well.

The FPSO is in this thesis assumed to be fixed. In reality, the impact will cause some motions for the FPSO as well. This can be implemented and will be more critical when the impact point has large eccentricities to the COG of the FPSO. As most ship collisions do not occur very close to the COG, this is important to investigate. In addition to this, more impact angles can be analyzed. For sharper impact angles, a longer part of the FPSO needs to be modeled.

The models in this thesis are verified to a satisfactory degree. However, more work can be done to determine the accuracy of the simulations. Different fracture models could be tested, in opposite to only the BWH-criterion used in this thesis. The effect of increased or decreased global size of the FPSO-model can also be examined. A possibility is to model the whole side between the transverse bulkheads, which will reduce the boundary condition uncertainty. A mesh convergence study should also be performed, both for the bow-model and the FPSO.

Different ship models and collision energies could be utilized. For example, a shuttle tanker, which has much higher collision energy than the OSV for the same impact

velocity. Different OSV-bow designs should also be investigated. For example, the X-Bow design does not have the same forecastle structure as a standard bow. Because the forecastle in this thesis is shown to dissipate a significant amount of energy, the X-Bow impact should be studied.

Bibliography

Abaqus, 2020. Abaqus Analysis User's Guide (6.14). URL: http://ivt-abaqusdoc.ivt.ntnu.no:2080/v6.14/books/usb/default.htm?startat=pt03ch06s03at08.html#usb-anl-aexpdynamic.

Alsos, H.S., Hopperstad, O.S., Törnqvist, R., Amdahl, J., 2008. Analytical and numerical analysis of sheet metal instability using a stress based criterion. International Journal of Solids and Structures 45, 2042–2055. URL: https://linkinghub.elsevier.com/retrieve/pii/S0020768307004817, doi:10.1016/j.ijsolstr.2007.11.015.

Arrieux, R., Bedrin, C., Bolvin, M., 1982. Determination of an Intrinsic Forming Limit Stress Diagram for Isotropic Metal Sheets. roceedings of the 12th Biennial Congress of the IDDRG , 62–71.

Bjørheim, C., 2017. Kollisjon på Ekofisk kunne blitt katastrofe. URL: https://www.aftenbladet.no/article/sa-yVRne.html.

Bressan, J., Williams, J., 1983. The use of a shear instability criterion to predict local necking in sheet metal deformation. International Journal of Mechanical Sciences 25, 155–168. URL: https://linkinghub.elsevier.com/retrieve/pii/0020740383900899, doi:10.1016/0020-7403(83)90089-9.

DNVGL-OS-C101, 2018. Design of offshore steel structures, general - LRFD method.

DNVGL-RP-C204, 2017. Design against accidental loads.

DNVGL-RP-C208, 2016. Determination of structural capacity by non-linear finite element analysis methods.

DNVGL-RP-F205, 2017. Global performance analysis of deepwater floating structures.

DNVGL-RU-Ship-Pt.6-Ch.6, 2019. Cold Climate.

FPSO.com, 2020. FPSO World Fleet – fpso.com. URL: http://fpso.com/fpso/.

Hill, R., 1952. On discontinuous plastic states, with special reference to localized necking in thin sheets. Journal of the Mechanics and Physics of Solids 1, 19–30. URL: http://www.sciencedirect.com/science/article/pii/0022509652900033, doi:10.1016/0022-5096(52)90003-3.

Kiendl, J., 2018. TMR 4190 Finite Element Methods in Structural Analysis - Lecture Notes.

Kvitrud, A., 2011. Collisions Between Platforms and Ships in Norway in the Period 2001-2010, in: Volume 2: Structures, Safety and Reliability, ASMEDC, Rotterdam, The Netherlands. pp. 637–641. URL: https://asmedigitalcollection.asme.org/OMAE/proceedings/OMAE2011/44342/637/341443, doi:10.1115/OMAE2011-49897.

Liu, Z., Amdahl, J., 2010. A new formulation of the impact mechanics of ship collisions and its application to a ship–iceberg collision. Marine Structures 23, 360–384. URL: https://linkinghub.elsevier.com/retrieve/pii/S0951833910000237, doi:10.1016/j.marstruc.2010.05.003.

Liu, Z., Amdahl, J., 2019. On multi-planar impact mechanics in ship collisions. Marine Structures 63, 364–383. URL: https://linkinghub.elsevier.com/retrieve/pii/S0951833918300947, doi:10.1016/j.marstruc.2018.10.006.

LS-Dyna, 2020. LS-DYNA User's Guide. URL: https://www.dynasupport.com/tutorial/ls-dyna-users-guide.

Lützen, M., Simonsen, B.C., Pedersen, P., 2000. Rapid Prediction of Damage to Struck and Striking Vessels in a Collision Event , 15.

MarineTraffic, 2020. MarineTraffic: Global Ship Tracking Intelligence | AIS Marine Traffic. URL: https://www.marinetraffic.com/no/ais/home/centerx:111.1/centery:43.6/zoom:2.

Minorsky, V., 1959. An Analysis of Ship Collisions With Reference to Protection of Nuclear Power Plants. Journal of Ship Research , 1–4.

Moan, T., 2003. Finite Element Modelling and Analysis of Marine Structures.

Moan, T., Amdahl, J., Ersdal, G., 2019. Assessment of ship impact risk to offshore structures - New NORSOK N-003 guidelines. Marine Structures 63, 480–494. URL: https://linkinghub.elsevier.com/retrieve/pii/S0951833917300904, doi:10.1016/j.marstruc.2017.05.003.

NORSOK-N001, 2004. Structural Design.

Pedersen, P., Zhang, S., 1998. On Impact mechanics in ship collisions. Marine Structures 11, 429–449. URL: https://linkinghub.elsevier.com/retrieve/pii/S0951833999000027, doi:10.1016/S0951-8339(99)00002-7.

Pedersen, P.T., Li, Y., 2009. On the global ship hull bending energy in ship collisions. Marine Structures 22, 2–11. URL: http://www.sciencedirect.com/science/article/pii/S0951833908000336, doi:10.1016/j.marstruc.2008.06.005.

Pettersen, E., Soegaard, L., 2005. A Study Of A Collision Incident Evaluated Against Ruling, in: Offshore Technology Conference, Offshore Technology Conference, Houston, Texas. URL: http://www.onepetro.org/doi/10.4043/17156-MS, doi:10.4043/17156-MS.

Pill, I., Tabri, K., 2011. Finite element simulations of ship collisions: a coupled approach to external dynamics and inner mechanics. Ships and Offshore Structures 6, 59–66. URL: https://doi.org/10.1080/17445302.2010.509585, doi:10.1080/17445302.2010.509585. publisher: Taylor & Francis _eprint: https://doi.org/10.1080/17445302.2010.509585.

Popov, Y.N., Faddeev, O.V., Kheisin, D.E., Yakovlev, A.A., 1969. STRENGTH OF SHIPS SAILING IN ICE. Technical Report FSTC-HT-23-96-68. ARMY FOREIGN SCIENCE AND TECHNOLOGY CENTER CHARLOTTESVILLE VA. URL: https://apps.dtic.mil/docs/citations/AD0684596.

Simonsen, B.C., Törnqvist, R., 2004. Experimental and numerical modelling of ductile crack propagation in large-scale shell structures. Marine Structures 17, 1–27. URL: https://linkinghub.elsevier.com/retrieve/pii/S0951833904000334, doi:10.1016/j.marstruc.2004.03.004.

Storheim, M., 2016. Structural Response in Ship-Platform and Ship-Ice Collisions , 388.

Storheim, M., Alsos, H.S., Amdahl, J., 2018. Evaluation of Nonlinear Material Behavior for Offshore Structures Subjected to Accidental Actions. Journal of Offshore Mechanics and Arctic Engineering 140, 041401. URL: https://asmedigitalcollection.asme.org/offshoremechanics/article/doi/10.1115/1.4038585/442724/Evaluation-of-Nonlinear-Material-Behavior-for, doi:10.1115/1.

4038585.

Stronge, W., 2004. Impact Mechanics. Cambridge University Press.

Tabri, K., 2012. Influence of coupling in the prediction of ship collision damage. Ships and Offshore Structures 7, 47–54. URL: http://www.tandfonline.com/doi/abs/10.1080/17445302.2011.553812, doi:10.1080/17445302.2011.553812.

Törnqvist, R., Technical University of Denmark, Department of Mechanical Engineering, 2003. Design of crashworthy ship structures. Ph.D. thesis. Department of Mechanical Engineering, Technical University of Denmark. Lyngby. OCLC: 473746266.

Yu, Z., Amdahl, J., 2016. Full six degrees of freedom coupled dynamic simulation of ship collision and grounding accidents. Marine Structures 47, 1–22. URL: https://linkinghub.elsevier.com/retrieve/pii/S0951833916300168, doi:10.1016/j.marstruc.2016.03.001.

Zhang, S., 1999. The Mechanics of Ship Collisions. Ph.D. thesis.

Appendices

Appendix A

Popov empirical equations

Popov et al. (1969) derived empirical equations for constant added masses and radii of gyrations for ships. These approximations are utilized in this thesis for analyzing the external dynamics of the ship collisions.

$$a_1 = 0 \tag{A.1}$$

In the thesis a_1 is set to 0.1, in agreement with supervisor.

$$a_2 = \frac{2T}{B} \tag{A.2}$$

$$a_3 = \frac{2}{3}\frac{BC_{wp}^2}{TC_b(1+C_{wp}} \tag{A.3}$$

$$a_4 = 0.25 \tag{A.4}$$

$$a_5 = \frac{B}{T(3-2C_{wp})(3-C_{wp}} \tag{A.5}$$

$$a_6 = 0.3 + 0.05\frac{L}{B} \tag{A.6}$$

$$R_{11}^2 = \frac{C_{wp}B^2}{11.4C_m} + H^2/12 \tag{A.7}$$

$$R_{22}^2 = 0.07C_{wp}L^2 \tag{A.8}$$

$$R_{33}^2 = L^2/16 \tag{A.9}$$

where a_i for i $\in$ [1,6] is the added mass in each degree of freedom and R_{ii} for i $\in$ [1,3] is the radius of gyration. T is the draft, B is the width, L is the length, C_{wp} is the water plane coefficient, C_m is the midship coefficient, C_b is the block coefficient and H is the height.

Appendix B

Figures from Storheim (2016)

Results from Storheim (2016) has been used for verification purpose of this thesis. The plots discussed in this thesis are presented in this section.

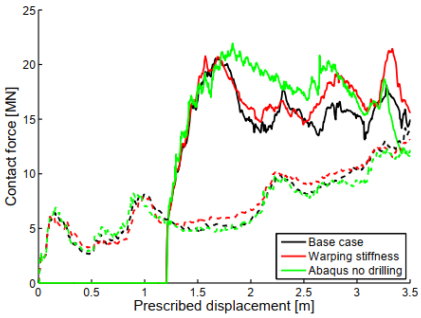

(a) Figure A17 from Storheim (2016)

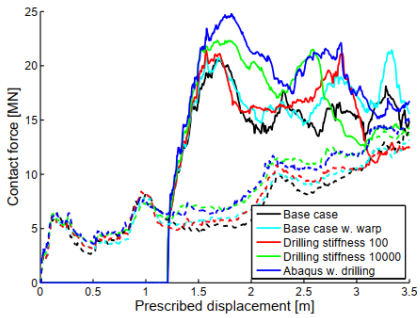

(b) Figure A18 from Storheim (2016)

Figure B.1: Comparison of Abaqus and LS-DYNA from Storheim (2016). All cases are from LS-Dyna except those specified as Abaqus.

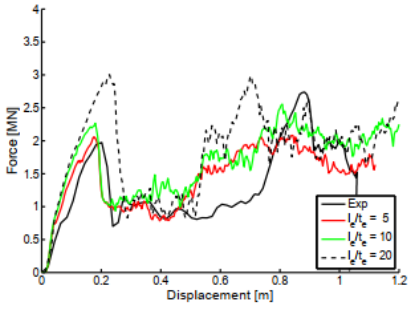

(a) BWH-fracture criterion

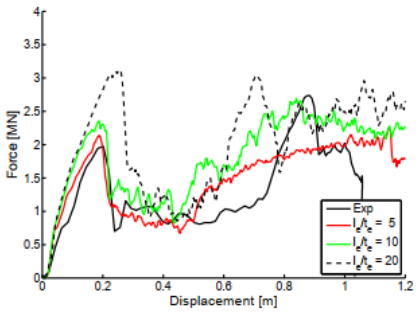

(b) RTCL-fracture criterion

Figure B.2: Fracture criterion comparison with experiments. Retrieved from Figure C.33 in Storheim (2016).

Appendix C

Analysis results

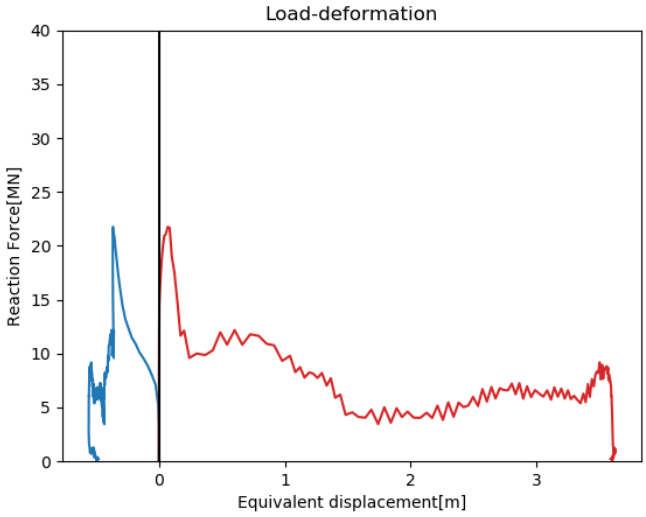

Figure C.1: Full load deformation curve for *ICE8*. Red is FPSO, and blue is OSV.

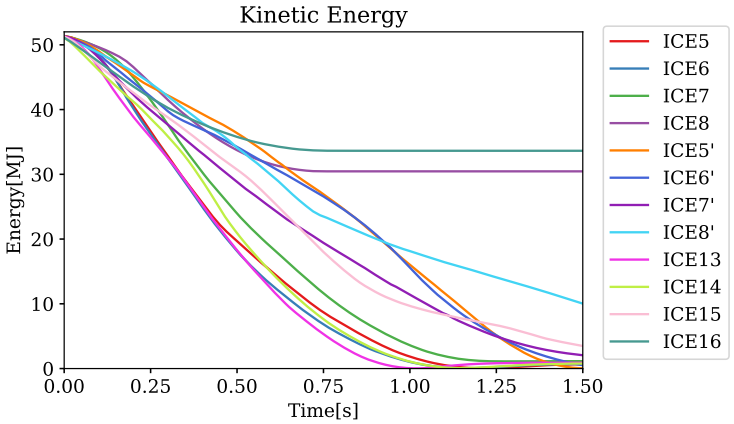

Figure C.2: Kinetic energy for all ICE-scenarios. Original modification of fully load condition noted" ' ".

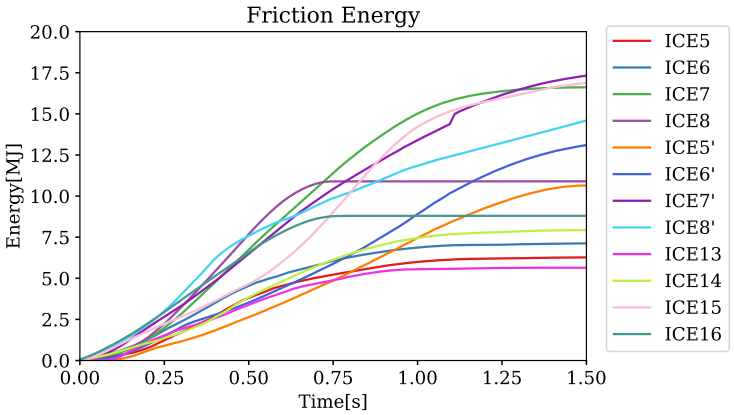

Figure C.3: Friction energy for all ICE-scenarios. Original modification of fully load condition noted" ' ".

Table C.1: Max penetration of FPSO-side for all scenarios

Scenario	Penetration [m]	% of side
SC 5	3.07	0.55
SC 6	2.88	0.51
SC 7	0.10	0.02
SC 8	0.19	0.03
SC 13	2.10	0.38
SC 14	1.80	0.32
SC 15	0.93	0.17
SC 16	0.00	0.00
ICE 5	1.99	0.36
ICE 6	1.92	0.34
ICE 7	1.24	0.22
ICE 8	0.00	0.00
ICE 13	0.83	0.15
ICE 14	1.17	0.21
ICE 15	0.36	0.06
ICE 16	0.00	0.00
ICE 5 ”	3.42	0.61
ICE 6 ”	3.31	0.59
ICE 7 ”	2.39	0.43
ICE 8 ”	1.25	0.22
SC 5 shifted	2.53	0.45
SC 6 shifted	2.39	0.43
SC 7 shifted	2.02	0.36
SC 8 shifted	0.35	0.06
SC 13 shifted	1.25	0.22
SC 14 shifted	0.99	0.18
SC 15 shifted	1.14	0.20
SC 16 shifted	0.00	0.00

Appendix D

Structural damage

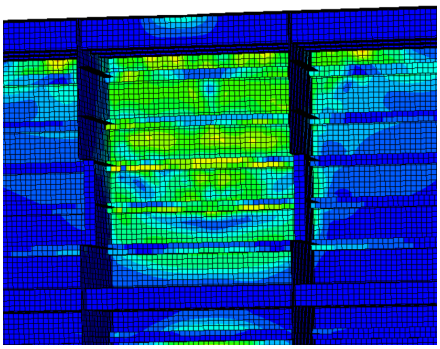

(a) *SC5*

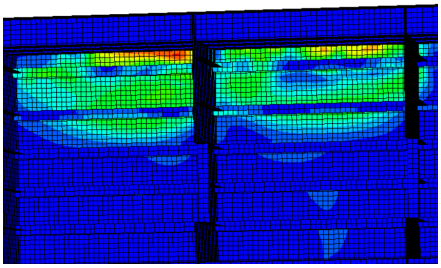

(b) *SC7*

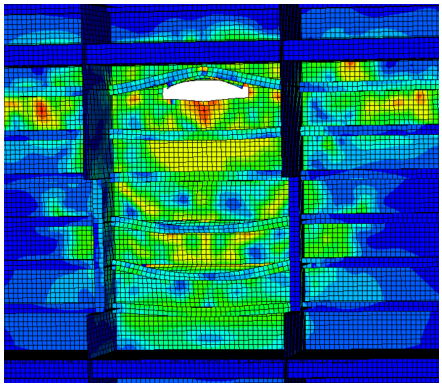

(c) *SC13*

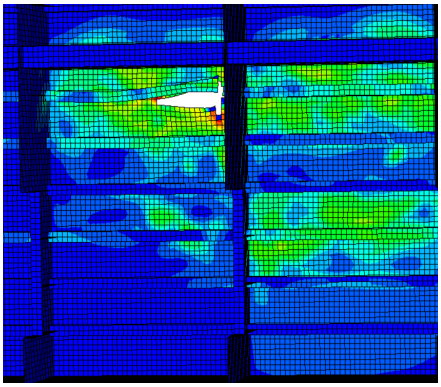

(d) *SC5*

Figure D.1: Structural damage from forecastle for selected scenarios. The view is from the back of the FPSO-side viewing towards the OSV.

Appendix E

External dynamics calculations

The procedure presented in Liu and Amdahl (2019) is used in this thesis. A comparison of the code written by the author and the result presented in Liu and Amdahl (2019) is shown below for both sticking impacts.

E.1 Verification result

Table E.1: Energy dissipation for sticking case from method presented in Liu and Amdahl (2019)

TestID	E_{Liu}	E_{Thesis}	Ratio	Case
101	1.25	1.25	1.00	stick
102	6.11	6.11	1.00	stick
103	6.84	6.84	1.00	stick
104	1.67	1.67	1.00	stick
105	3.60	3.60	1.00	stick
106	5.50	5.49	1.00	stick
107	6.80	6.79	1.00	stick
108	5.21	5.19	1.00	stick
109	1.53	1.52	0.99	stick
110	5.56	5.54	1.00	stick
111	8.13	7.85	0.97	stick
112	7.79	7.67	0.98	stick
113	2.56	2.51	0.98	stick

E.2 Python scripts

E.2.1 multiplanar.py

```
"""
---------------External dynamics main script------------------
-------------------------------------------------------------
Based on the paper "On multi-planar impact mechanics in ship
collisions"
by Zhenhui Liu and Jørgen Amdahl(2019).

Input: ship coefficients from coefficients.py

Returns: Energy dissipated in each principal direction

Note: The slide case is not verified, and is not probable to give
correct results

Script made by: Lasse Tellevik, June 2019
"""

import numpy as np
import math
import coefficients as coeff

#Input parameters, ship data are imported from the subroutine
coefficients.py
mu_0=0.6
alfa=0 #degrees for midships
beta=0 #degrees for midships
Theta=np.array([90])#,75,60,45]) #head-on impact
v_b=np.array([[0,0,0]]) #Ship A velocity in body-coord
v_b1=np.array([[3.5,0,0]]) #Ship B velocity in body-coord
r_b=np.array([0,0,0]) #Impact point in A-coord, y can be changed
e=0 #Restituion factor

#Declaration of variables
c=0 #counter
case=['']*len(Theta)
E1=np.zeros((len(Theta),1))
E2=np.zeros((len(Theta),1))
E3=np.zeros((len(Theta),1))


##-------------------Step 1-----------------------------------------
#Establish the-body-fixed coordinate systems for ships A and A'
#and the local impact coordinate system

#Unit vectors in body-fixed coord system
A=np.array([[1,0,0],[0,1,0],[0,0,1]]) #Ship A
A1=A #Ship A'
```

```
L=A #Unit vectors for local coord system

##-------------------Step 2-----------------------------------------
#Calculate direction cosines l_i'.... n_i'
#Running script for all angles in theta
for theta in Theta:
    cos_a=math.cos(math.radians(alfa)) #cosine in degrees for alfa
    sin_a=math.sin(math.radians(beta)) #sine in degrees for alfa
    cos_b=math.cos(math.radians(beta)) #cosine in degrees for beta
    sin_b=math.sin(math.radians(beta)) #sine in degrees for beta
    cos_t=math.cos(math.radians(theta))
    sin_t=math.sin(math.radians(theta))

    #Transform from A to A'
    T_b_b1=np.array([[cos_t,sin_t,0],[-sin_t,cos_t,0],[0, 0, 1]])
    #Transform from A' to A'
    T_b1_b=T_b_b1.transpose()
    #Transform from A to local
    T_b_n=np.array([[cos_a,-sin_a,0],[-sin_a*sin_b, -cos_a*sin_b,
    -cos_b],
                    [ sin_a*cos_b,  cos_a*cos_b, -sin_b]])
    #Transform from A' to local
    T_b1_n=np.dot(T_b_n,T_b1_b)

##-------------------Step 3-----------------------------------------
    #Calculate relative velocity before impact under the local
    coordinate system
    #Velocity for A in body-coordinate system
    v_0=np.dot(T_b_n,v_b.transpose())
    #Velocity for A' in body-coordinate system
    v1_0=np.dot(T_b1_n,v_b1.transpose())
    #Relative velocity
    vrel_0=v_0-v1_0

##-------------------Step 4-----------------------------------------
    #Importing constants
    #Ship A (FPSO)
    m,a1,a2,a3,a4,a5,a6,R1,R2,R3,L=coeff.coefficients('FPSO')
    #Added mass coefficients
    a=np.array([a1,a2,a3,a4,a5,a6])
    #Radii of gyration squared
    R=np.array([R1,R2,R3]) #[m^2]

    #Ship A'(OSV)
    m1,a1,a2,a3,a4,a5,a6,R1,R2,R3,L1=coeff.coefficients('OSV')
    #added mass coefficients
    a1=np.array([a1,a2,a3,a4,a5,a6])
    #Radii of gyration squared
    R1=np.array([R1,R2,R3]) #[m^2]

    #Defining impact point for ship A'
    r_b1=np.array([L1/2,0,4])
```

```
94
95      #Calculate reduction matrices Cn and C'n
96      r_b_star=np.array([[0,-r_b[2], r_b[1]],r_b[2],0,-r_b[0]],
97          [-r_b1[1], r_b1[0], 0]])
98      r_b1_star=np.array([[0,-r_b1[2], r_b1[1]],[r_b1[2],0,-r_b1[0]],
99          [-r_b1[1], r_b1[0], 0]])
100     #Lever arm matrix for A and A'
101     D_n=np.dot(T_b_n,r_b_star)#[o_i,p_i,q_i].....
102     D1_n=np.dot(T_b1_n,r_b1_star)
103
104     #-----Reduction factor matrix----
105     C=np.zeros((3,3)) #Ship A
106     C1=np.zeros((3,3)) #Ship A'
107
108     for i in range(0,3):
109         for j in range(0,3):
110             C[i,j]=T_b_n[i][0]*T_b_n[j][0]/(1+a[0])+\
111                 T_b_n[i][1]*T_b_n[j][1]/(1+a[1])+\
112                 T_b_n[i][2]*T_b_n[j][2]/(1+a[2])+\
113                 D_n[i][0]*D_n[j][0]/((1+a[3])*R[0])+\
114                 D_n[i][1]*D_n[j][1]/((1+a[4])*R[1])+\
115                 D_n[i][2]*D_n[j][2]/((1+a[5])*R[2])
116
117             C1[i,j]=T_b1_n[i][0]*T_b1_n[j][0]/(1+a1[0])+\
118                 T_b1_n[i][1]*T_b1_n[j][1]/(1+a1[1])+\
119                 T_b1_n[i][2]*T_b1_n[j][2]/(1+a1[2])+\
120                 D1_n[i][0]*D1_n[j][0]/((1+a1[3])*R1[0])+\
121                 D1_n[i][1]*D1_n[j][1]/((1+a1[4])*R1[1])+\
122                 D1_n[i][2]*D1_n[j][2]/((1+a1[5])*R1[2])
123
124 ##-------------------Step 5-----------------------------------------
125     #Assemble the collision matrix
126     K_n=np.zeros((3,3))
127
128     for i in range(0,3):
129         for j in range(0,3):
130             K_n[i,j]=C[i,j]/m+C1[i,j]/m1
131
132 ##-------------------Step 6-----------------------------------------
133     #Solve to obtain the impulse S_n
134     K_n_inv=np.linalg.inv(K_n)
135     #Relative velocity change during impact
136     dv=[-vrel_0[0,0],-vrel_0[1,0],-(1+e)*vrel_0[2,0]]
137     #Impulse matrix
138     S=np.dot(K_n_inv,dv)
139
140 ##-------------------Step 7-----------------------------------------
141     #Calculate the friction factors
142     mu_n=np.sign(S[0])*math.sqrt(S[0]**2+S[1]**2)/S[2]
143     mu_t=S[1]/S[0]
144     mu_1=S[0]/S[2]
145     mu_2=S[1]/S[2]
```

```
##-------------------Step 8----------------------------------------
    #Stick case
    if abs(mu_n)<abs(mu_0):
        E1[c,0]=0.5*mu_1/(mu_1*K_n[0,0]+mu_2*K_n[0,1]+
                          K_n[0,2])*(1-e**2)*(vrel_0[0,0])**2
        E2[c,0]=0.5*mu_2/(mu_1*K_n[1,0]+mu_2*K_n[1,1]+
                          K_n[1,2])*(1-e**2)*(v_0[1,0]-v1_0[1,0])**2
        E3[c,0]=0.5*1/K_n[2,2]*(1-e**2)*(vrel_0[2,0])**2
        case[c]='stick'

    #Slide case
    else:
         mu_n=mu_0
         #Relative velocity changes
         dv1=-(mu_1*K_n[0,0]+mu_2*K_n[0,1]+K_n[0,2])/
                (mu_1*K_n[2,0]+mu_2*K_n[2,1]+K_n[2,2])*(vrel_0[2,0])
         dv2=-(mu_1*K_n[1,0]+mu_2*K_n[1,1]+K_n[1,2])/
                (mu_1*K_n[2,0]+mu_2*K_n[2,1]+K_n[2,2])*(vrel_0[2,0])
         dv=[dv1,dv2,-vrel_0[2,0]]
         v1_t=vrel_0[0,0]+dv[0]
         v2_t=vrel_0[1,0]+dv[1]

         E1[c,0]=0.5*mu_1/(mu_1*K_n[0,0]+mu_2*K_n[0,1]+
                K_n[0,2])*abs((2*vrel_0[0,0]+dv1)*dv1)
         E2=0.5*mu_2/(mu_1*K_n[1,0]+mu_2*K_n[1,1]+
                K_n[1,2])*abs((2*vrel_0[1,0]+dv2)*dv2)
         E3[c,0]=0.5*1/(mu_1*K_n[2,0]+
                 mu_2*K_n[2,1]+K_n[2,2])*vrel_0[2,0]**2
         case[c]='slide'
    c=c+1
```

E.2.2 coefficients.py

```
"""
------------coefficients.py-----------------------------
--------------------------------------------------------
Coefficients for external dynamic script.
The calculations are based on Popov emprical factors.

Imports model parameters from OSVdata.py and FPSOdata.py

Returns mass, length, added mass and radii of gyrations

Script made by: Lasse Tellevik, June 2019
"""
def coefficients(object):
    #if object=! 'FPSO' or object!= 'OSV':
     #   return false
    if object=='OSV':
```

```
        import OSVdata as model
    elif object=='FPSO':
        import FPSOdata as model

    #Popov empirical equations
    a1=0.1; #Added mass in 1-dir, decided to be 0.1 instead of 0
    a2=2*model.T/model.B;
    a3=((2/3)*(model.B*model.Cwp**2))/(model.T*model.Cb*(1+model.Cwp))
    a4=0.25
    a5=model.B/(model.T*(3-2*model.Cwp)*(3-model.Cwp))
    a6=0.3+0.05*model.L/model.B

    #Radii of gyration squared
    R1=model.Cwp*model.B**2/(11.4*model.Cm)+model.H**2/12
    R2=0.07*model.Cwp*model.L**2
    R3=model.L**2/16

    return model.m,a1,a2,a3,a4,a5,a6,R1,R2,R3,model.L
```

E.2.3 OSVdata.py

```
"""
------------OSVdata.py----------------------------------
--------------------------------------------------------
Defines data for calculating OSV coefficients

Script made by: Lasse Tellevik, June 2019
"""

#Main dimensions OSV
L=78.8 #length between perpendiculars
B=18.8 #breadth
depth=7.6 #moulded depth
T=6.2 #draught
rho=1025 #[kg/m^3]
g=9.81 #[m/s^2]
m=7.5e6 #[kg], mass
Cb=m/(L*B*T*rho)
GM=1 #m assumed

#Coefficients
#Waterplane coefficient
Al=86 #approximated length of waterplanearea
L_tria=20 #length of triangular shape at front
A_square=Al*B
Awp=Awp=A_square-L_tria*B/2
Cwp=Awp/A_square #Waterplane coefficient
```

```
27
28 #Midship coefficient
29 Am_square=B*depth
30 Am=Am_square-(18.8-16.6)*1.8 #1.8=h tanktop
31 Cm=Am/Am_square #Approximate to 0.95
32 H=depth
```

E.2.4 FPSOdata.py

```
1  """
2  -------------FPSOdata.py----------------------------------
3  ----------------------------------------------------------
4  Defines data for calculating FPSO coefficients
5
6  Script made by: Lasse Tellevik, June 2019
7  """
8
9  #Main dimensions OSV
10 L=295 #length between perpendiculars
11 B=58 #breadth
12 depth=31 #moulded depth
13 T=24 #draught
14 rho=1025 #[kg/m^3]
15 g=9.81 #[m/s^2]
16 Cb=0.85
17 m=Cb*L*B*T*rho #[kg], mass
18 GM=1 #m assumed
19
20 #Coefficients
21 #Waterplane coefficient
22 Al=295 #approximated length of waterplane area
23 L_tria=40 #length of triangular shape at front
24 A_square=Al*B
25 Awp=Awp=A_square-L_tria*B/2
26 Cwp=Awp/A_square #Waterplane coefficient
27
28 #Midship coefficient
29 Am_square=B*depth
30 Am=Am_square-3.5*3.2
31 Cm=Am/Am_square #Approximate to 0.95
32 H=30
```

Appendix F

FPSO model

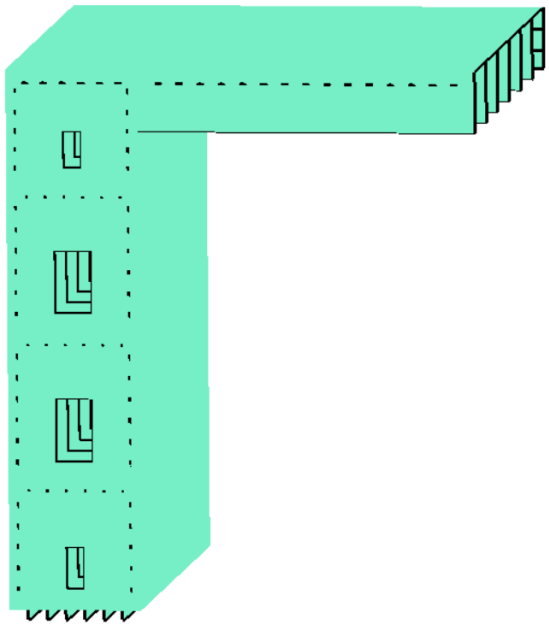

Figure F.1: Free edges of the FPSO model, showing only stiffener flanges are free to move through transverse web frame.

Lasse Tellevik

Analyses of ship collisions between an FPSO and an OSV

NTNU
Norwegian University of
Science and Technology